

The atomizing pulsed jet

Yash Kulkarni^{1†}, Cesar Pairetti^{1‡}, Raphaël Villiers¹, Stéphane Popinet¹ and Stéphane Zaleski^{1,2p}

¹Sorbonne Université and CNRS, UMR 7190, Institut Jean Le Rond d'Alembert, 75005 Paris, France

²Institut Universitaire de France, UMR 7190, Institut Jean Le Rond d'Alembert, 75005 Paris, France

(Received xx; revised xx; accepted xx)

Direct Numerical Simulations of the injection of a pulsed round liquid jet in a stagnant gas are performed in a series of runs of geometrically progressing resolution. The Reynolds and Weber numbers and the density ratio are sufficiently large for reaching a complex high-speed atomization regime but not so large so that the small length scales of the flow are impossible to resolve, except for very small liquid-sheet thickness. The Weber number based on grid size is then small, an indication that the simulations are very well resolved. Computations are performed using octree adaptive mesh refinement with a finite volume method and height-function computation of curvature, down to a specified minimum grid size Δ . Qualitative analysis of the flow and its topology reveals a complex structure of ligaments, sheets, droplets and bubbles that evolve and interact through impacts, ligament breakup, sheet rupture and engulfment of air bubbles in the liquid. A rich gallery of images of entangled structures is produced. Most processes occurring in this type of atomization are reproduced in detail, except at the instant of thin sheet perforation or breakup. We analyze droplet statistics, showing that as the grid resolution is increased, the small-scale part of the distribution does not converge, and contains a large number of droplets close in order of magnitude to the minimum grid size with a significant peak at $d = 3\Delta$.

This non-convergence arises from the *numerical sheet breakup* effect, in which the interface becomes rough just before it breaks. The rough appearance of the interface is associated to a high-wavenumber oscillation of the curvature. To recover convergence, we apply the controlled “manifold death” numerical procedure, in which thin sheets are detected, and then pierced by fiat before they reach a set critical thickness h_c that is always larger than 6Δ . This allows convergence of the droplet frequency above a certain critical diameter d_c above and close to h_c . A unimodal distribution is observed in the converged range.

Key words:

1. Introduction

Atomization simulations have progressed at an amazing rate, however the topic is still far from mature. As we shall show in this paper the prediction of the breakup

† Email address for correspondence: kulkarniyash2398@gmail.com

‡ Email address for correspondence: paire.cesar@gmail.com

p Email address for correspondence: stephane.zaleski@sorbonne-universite.fr

of liquid masses in a typical large-speed flow is marred by vexing numerical effects and profound physical uncertainties. New developments, such as better codes, rapidly increasing processing power and new numerical methods are however poised to mitigate the difficulties. In this paper, we investigate the pulsed jet, a paradigmatic case of atomizing flow inspired by diesel engine jets, although we do not aim at solving a particular applied problem or even any experimental configuration, but rather to investigate the potential and limitations of Direct Numerical Simulation (DNS) of atomising flow, and in particular the ability of such DNS to reveal physically relevant properties of the flow through *statistically converged* numerical approaches. The emphasis here is on statistical convergence, rather than “trajectory” convergence, since only the former is conceivable in very complex, irregular flows.

The study of such convergence already has a long history, despite rapid progress. We review specifically the history of round jet atomizing simulations and we refer the reader to reviews on the general topic of atomization and its simulation (Gorokhovski & Herrmann 2008; Villermaux 2020). The first attempts at testing the convergence of the Probability Distribution Function (PDF) of droplet sizes were those of Herrmann (2011). His simulations of a round jet used a variant of the Level-Set method and showed that the number of small droplets in the PDF was underestimated by coarse-grid simulations. This can be understood by the fact the the Level-Set methods tend to eliminate small droplets by “evaporating” them. On the other hand Volume-Of-Fluid (VOF) methods keep too many droplets in an intermediate range around the grid size Δ , and in that range the PDF of droplet sizes is overestimated. This can be seen for example in a study of the convergence of the droplet size distribution in the round jet by Pairetti *et al.* (2020) where coarse grids overestimate the number of large droplets.

A graphical illustration of the contrasting effects of Level-Set and VOF methods on the droplet sizes in atomization is shown on Figure 1. Despite the inaccuracy of the distribution for small droplet diameters, both methods may converge as the grid is refined progressively. There is thus some hope that very large simulations will eventually produce converged distributions, a hope we want to explore in this paper.

Aside from the two investigations cited above, very few studies address the issue of PDF convergence, despite detailed analyses of aspects of the flow. Perhaps the first round, single-jet atomization simulation in the conditions of a diesel jet was that of Bianchi *et al.* (2005) using the VOF method, followed by more detailed simulations by Ménard *et al.* (2007) using the Combined Level-Set VOF method (CLSVOF). This was followed by other simulations using CLSVOF by Lebas *et al.* (2009), Chesnel *et al.* (2011) and Anez *et al.* (2019) and by simulations using the VOF method (Fuster *et al.* 2009). The latter studied both the coaxial jet cases in the so-called “assisted atomization” setup and the conical jet. For the conical jet Fuster *et al.* (2009) showed that the PDF changed drastically with grid resolution. The PDF never peaked as the droplet size was decreased towards the grid size. Until 2022, the most detailed (or highest-fidelity) published simulations of a round jet were performed by Shinjo & Umemura (2010) using a combination of Level-Set and VOF techniques with a ratio of jet diameter to grid size of 286. These simulations, together with those of Herrmann (2011) are the two outliers above the trend line in Figure 2. In addition to revealing a wealth of details about ligament and sheet formation, and the perforation of sheets, Shinjo & Umemura have also shown distributions of droplet sizes, but without investigating explicitly their convergence. As in earlier simulations of the round jet, the droplet size distribution has a single maximum close to the small droplet end of the spectrum, almost at the grid size. Studies by Jarrahbashi & Sirignano (2014); Jarrahbashi *et al.* (2016) focused on a round, spatially-periodic jet and analyzed the effect of vortex dynamics on the development of

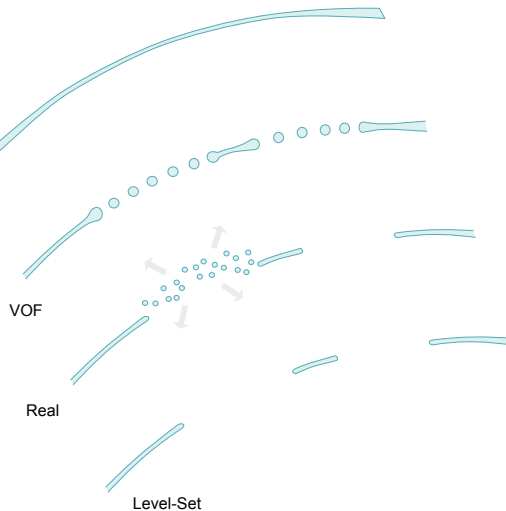


FIGURE 1. An illustration of the outcomes for the numerical simulation of a thinning liquid sheet. The Volume of Fluid method breaks when the sheet thickness reaches the grid size. Because of mass conservation fragments larger than the grid size are obtained. The Level-Set or Diffuse-Interface method on the other hand evaporates the thin parts of the sheet. In reality, the sheet thinning would continue until the sheet is much thinner, unless extremely fine grids are used. The final size of some of the droplets would then be much smaller than in the VOF simulation.

instabilities along with the jet core. Studies by Zhang *et al.* (2020) and Pairetti *et al.* (2020) applied the VOF method with octree Adaptive Mesh Refinement. As already mentioned the later paper investigated the distribution of droplet sizes showing some difficulties in reaching statistical convergence. Several authors including Torregrosa *et al.* (2020) and Salvador *et al.* (2018) have focused on the effect of injection conditions and turbulence. Khanwale *et al.* (2022) and Saurabh *et al.* (2023), using a diffusive interface method with octree Adaptive Mesh Refinement, obtained the most refined simulations published at time of writing with a special treatment of the refinement in thin regions. It should be noted that all of the round-jet studies cited above involve a variety of physical parameters and grid resolutions, despite the fact that they share similarities, such as moderate density ratios and liquid Reynolds numbers (defined below) in a range $5000 \leq Re_l \leq 13400$ that are attainable by Direct Numerical Simulation for single-phase flow. For example the two octree studies of Zhang *et al.* (2020) and Pairetti *et al.* (2020) have gas-based Weber numbers (defined below) of respectively 177 and 417. As a general rule, it is better to select relatively small density ratios, Reynolds and Weber numbers to increase the likelihood of reaching convergence in computation. In this work, we thus chose the parameters in the lower range of Re , We and density ratio for this type of flow. Similar attempts at obtaining convergence were realized in the simulations of Ling *et al.* (2017), investigating assisted quasi-planar atomization after the experiment of Grenoble (Ben Rayana *et al.* 2006; Fuster *et al.* 2013). Ling *et al.* (2017) performed computations on four grids of increasing resolution. Despite the huge computational effort involved in that latter simulation, convergence was clearly not reached, both quantitatively as droplet size distributions had a very narrow region of overlap, and qualitatively as clearly under-resolved structures in thin sheet-like regions were observed. One of our objectives in this work is to see what happens if ever finer grids are used, until very thin sheets are clearly

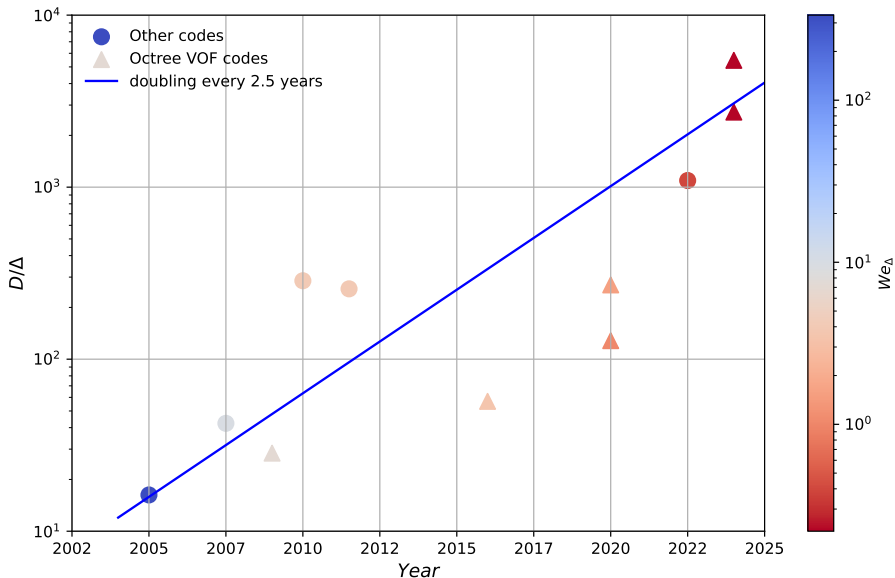


FIGURE 2. The increase in two-phase round-jet grid resolution in time. The graph includes two simulations published only on the Gerris and Basilisk websites (and in other channels outside of academic journals) before 2017. The 2024 simulations are those reported in this paper.

resolved. In experiments as well as in some simulations it is clear that thin sheets are the site of weak spots (Lohse & Villermaux 2020). The presence of these weak spots as one of the mechanisms leading to atomization forces the following somewhat sobering conclusion. Numerical simulations of Diffuse-Interface, Level-Set or VOF type can never be converged if thin sheets break or perforate only when they reach the grid size. Instead a physical mechanism for weak spots or perforations must be present to nucleate holes in a manner independent of the numerics. Although such a mechanism may not be known yet, we suggest as a backstop procedure to define a critical sheet thickness h_c beyond which perforations occur with relatively high frequency, that is at the rate of one or more perforations per connected thin-sheet region. Chirco *et al.* (2022) have called *manifold death* (MD) this procedure[†]. It should be noted that bags or membranes are observed at relatively low velocities in many atomization configurations (droplets, jets etc...) and that at higher velocities, bags are not visible and perhaps non existent. We note that the literature (Lasheras & Hopfinger 2000) distinguishes two kinds of atomization, a bag or membrane-type atomization at $We_g < 200$ and a fiber-type atomization at higher values of the Weber number. From the connection between thin sheets and the lack of statistical convergence one may conjecture that in the fiber-type regime statistical convergence could be achieved. This is however contradicted by the lack of convergence observed by Herrmann (2011) at $We_g = 500$. A definite answer to this argument may have to wait for a study similar to the one in this paper in the fiber type regime, a study which would probably be even more expensive.

In what follows we first describe the characteristics of our test case. We then describe our numerical method, including the manifold death (MD) procedure. Then we continue with our results, which are both qualitative, revealing new processes of numerical rupture, and quantitative based on analysis of the droplet size distributions. A sketchy discussion

[†] This choice of words partially echoes that of Debrégeas *et al.* (1998).

of the physical phenomenology of hole expansion in a thin sheet is discussed in Appendix A. We end with a conclusion including perspectives and discussion.

2. Mathematical model and numerical method

Our mathematical model is based on the mass and momentum-conservation equations for incompressible and isothermal flow

$$\nabla \cdot \mathbf{u} = 0, \quad (2.1)$$

$$\frac{\partial \rho \mathbf{u}}{\partial t} + \nabla \cdot (\rho \mathbf{u} \mathbf{u}) = -\nabla p + \nabla \cdot (2\mu \mathbf{D}) + \mathbf{f}_\sigma, \quad (2.2)$$

where $\mathbf{u}(\mathbf{x}, t)$ is the velocity field and $p(\mathbf{x}, t)$ is the pressure field. The tensor \mathbf{D} is defined as $\frac{1}{2} [\nabla \mathbf{u} + (\nabla \mathbf{u})^T]$. The density and viscosity of the flow are noted as ρ and μ respectively. The last term on the right-hand side of the Navier–Stokes Equation (2.2) represents the surface tension force

$$\mathbf{f}_\sigma = \sigma \kappa \mathbf{n} \delta_s, \quad (2.3)$$

which depends on the surface tension σ and the interface shape, particularly on its curvature κ and unit normal vector \mathbf{n} . The Dirac distribution δ_s indicates that the force only acts at the free surface. We consider the phase distribution function $c(\mathbf{x}, t)$ that takes value unity in the reference phase and null outside of it. The transport equation for this function is:

$$\frac{\partial c}{\partial t} + \nabla \cdot (c \mathbf{u}) = c \nabla \cdot \mathbf{u}. \quad (2.4)$$

In the context of incompressible flow, the right-hand side above is equal to zero. The c function implicitly defines the interface at its discontinuity surface, defining also the δ_s , \mathbf{n} , and κ fields, e.g. $\nabla c = \mathbf{n} \delta_s$.

The Volume of Fluid method represents the evolution of c using the Piecewise Linear Interface Capturing (PLIC) method of Hirt & Nichols (1981) and DeBar (1974). In this context, the mean value of the color function on a cell is

$$f = \frac{1}{|\Omega|} \int_{\Omega} c(\mathbf{x}, t) dV, \quad (2.5)$$

where $|\Omega|$ is the volume of the cell Ω . Then f is the volume fraction of the reference phase in the cell. The mixture properties of the cell may then be computed by arithmetic averages

$$\rho_\Omega = f \rho_l + (1 - f) \rho_g, \quad \mu_\Omega = f \mu_l + (1 - f) \mu_g. \quad (2.6)$$

Spatial discretization of the above Equation is realized on a network of cubic cells obtained by a tree-like subdivision of an initial cubic cell of size L_0 . The subdivision is realized using a wavelet based error estimate and is adapted dynamically as the simulation progresses. At all times the maximum subdivision level is a fixed number ℓ and the smallest grid size is

$$\Delta_\ell = 2^{-\ell} L_0 / 3. \quad (2.7)$$

From now on, we consider the algebraic equations derived from applying the Finite Volume Method on each cell. In this context, the approximate projection method by Chorin (1968) can be used to solve the coupling between equations (2.1) and (2.2), considering that the velocity \mathbf{u} is staggered in time with respect to the volume fraction

f and the pressure p . The discrete set of equations can then be expressed as

$$\frac{\rho \mathbf{u}^* - \rho \mathbf{u}^n}{\Delta t} + \nabla \cdot \left(\rho^{n+\frac{1}{2}} \mathbf{u}^{n+1/2} \mathbf{u}^{n+1/2} \right) = \nabla \cdot [\mu^{n+\frac{1}{2}} (\mathbf{D}^n + \mathbf{D}^*)] + \mathbf{f}_\sigma^{n+1/2} \quad (2.8)$$

$$\nabla \cdot \left(\frac{\Delta t}{\rho^{n+\frac{1}{2}}} \nabla p^{n+\frac{1}{2}} \right) = \nabla \cdot \mathbf{u}^* \quad (2.9)$$

$$\mathbf{u}^{n+1} = \mathbf{u}^* - \frac{\Delta t}{\rho^{n+\frac{1}{2}}} \nabla p^{n+\frac{1}{2}} \quad (2.10)$$

In the above the expression $\nabla \cdot \left(\rho^{n+\frac{1}{2}} \mathbf{u}^{n+1/2} \mathbf{u}^{n+1/2} \right)$ must be interpreted as the use of a predictor-corrector scheme for advection of the velocity field. Both the predictor and the corrector use the Bell-Collela-Glaz scheme (Popinet 2003, 2009), and involve two projections. A full description of the predictor corrector scheme with projection is best found in the ‘‘literate’’ source code <http://basilisk.fr/src/navier-stokes/centered.h>. In addition to these equations, f is advanced in time using the split-volume-fraction advection scheme of Weymouth & Yue (2010). We use the semi-implicit Crank-Nicholson scheme to compute the diffusive flux due to the viscous term in Equation (2.8). An important aspect of the method is the resolution of the surface tension force \mathbf{f}_σ . We use the Continuous Surface Force (CSF) well-balanced formulation $\mathbf{f}_\sigma = \sigma \kappa \nabla c$ for Eq. 2.3. where we discretize ∇c at cell faces with the same scheme employed to compute the pressure gradient ∇p . This is useful to reduce spurious currents provided curvature is accurately computed, as explained by Popinet (2018, 2009). The interface curvature is computed using second-order stencils based on height functions (Popinet 2009; Bornia *et al.* 2011). Equations (2.9) and (2.10) are the projection steps that will ensure continuity for the velocity field at time step $n+1$. The mesh is adapted dynamically, by splitting the grid cells to eight smaller cells whenever the estimated local discretization error exceeds a set threshold (see Appendix B). Details of the procedure can be found on the web site basilisk.fr, and in particular in the documented free code <http://basilisk.fr/src/examples/atomisation.c>.

In addition to the aforementioned model and procedure, we implement the *manifold-death* procedure as described by Chirco *et al.* (2022). This procedure involves two primary steps: (1) the identification of thin liquid sheets with a thickness of h_c or less, achieved through a local integration of the characteristic function c . This integration results in the signature of a quadratic form, based on the local main inertia moments; (2) the creation of holes within the so identified thin sheets, using a probabilistic approach. This procedure is applied at a given frequency, defined by the user within this method. From a physical standpoint, this technique aligns with the weak spot model, wherein the likelihood of hole formation is exceedingly low for $h > h_c$ and substantially increases, rapidly approaching certainty, for $h < h_c$. The complete manifold death code can be accessed at <http://basilisk.fr/sandbox/lchirco/signature.h>. In the present case hole punching is attempted every time interval of $\tau_m = 0.01$. At these instants 200 holes are attempted. As we show in Appendix A the characteristic time for sheet thinning is τ_c given by

$$\tau_c = \frac{D}{U} \left(\frac{\rho_l}{\rho_g} \right)^{1/2}. \quad (2.11)$$

The dimensionless interval between punching attempts is $\tau_m/\tau_0 = 0.01$ where the dimensioning factor is $\tau_0 = 3L_0/U$ for all time values in our simulations. The dimensioning

Re_l	We_g	ρ^*	μ^*	A_p	ω_p	L_0/D
5800	200	27.84	27.84	0.05	$\pi/5$	18

TABLE 1. The dimensionless numbers characterizing our simulation. The Reynolds number Re_l based on the liquid is rather moderate. The density and viscosity ratios are identical, which implies that $\text{Re}_g = \text{Re}_l$.

quantities L_0 and D/L_0 are defined below. Then we have

$$\tau_m/\tau_c = 0.06 \left(\frac{\rho_g}{\rho_l} \right)^{1/2} \quad (2.12)$$

The numerical value is $\tau_m/\tau_c = 0.011$ ensuring that punching attempts are sufficiently frequent as not to “miss” transient thinning sheets.

Using this numerical method, we analyze the atomization of a circular jet injected at average velocity U in a gas-filled cubical chamber of edge length L_0 considering incompressible isothermal flow. The dimensionless groups most relevant for this problem are the gas-based Weber number, the liquid-based Reynolds number and the ratios

$$\text{We}_g = \frac{\rho_g U^2 D}{\sigma}, \quad \text{Re}_l = \frac{\rho_l U D}{\mu_l}, \quad \rho^* = \frac{\rho_l}{\rho_g}, \quad \mu^* = \frac{\mu_l}{\mu_g}, \quad \frac{L_0}{D}, \quad (2.13)$$

where ρ_l and ρ_g are the densities of liquid and gas respectively. The viscosity coefficients are noted by μ_l and μ_g , and σ is the surface tension coefficient. All the numerical values for time given in the paper are made dimensionless by $L_0/(3U)$ and all length values are dimensioned by $L_0/3$. The boundary condition on the injection plane $x = 0$ imposes the no-slip condition everywhere except on the liquid section ($y^2 + z^2 < D^2/4$) where the injection velocity is:

$$u_x(t) = U [1 + A_p \sin(\omega_p U t / D)]. \quad (2.14)$$

On the remaining cube sides, we allow free outflow: $\partial_n \mathbf{u}_\Gamma = 0$ and $p_\Gamma = 0$.

The dimensionless parameters of our simulation are given in Table 1. These numbers are in the low range of the dimensionless numbers used in the above cited work. They are much smaller than the numbers of the spray G case of the Engine Combustion Network (see Duke *et al.* (2017) used by Zhang *et al.* (2020). The Reynolds number and density ratio are identical to those of Ménard *et al.* (2007) and of the same order as those of Herrmann (2011). On the other hand the Reynolds number is somewhat larger than that of Shinjo & Umemura (2010) while the gas Weber number We_g is smaller than that of all the other papers in the literature. The rationale for selecting such a small Weber number is twofold. First the simplest prediction for the droplet size, based on the ratio of Bernoulli pressure $\rho_g U^2$ to surface tension, is $d = D \text{We}_g^{-1}$. Indeed if a purely inviscid flow with a velocity jump is considered, the cutoff wavelength for the Kelvin-Helmholtz instability scales as $D \text{We}_g^{-1}$. The wavelength thus obtained is a natural scale for the subsequent formation of sheets and ligaments. The number of grid points in the diameter of a droplet of this diameter d is then We_Δ^{-1} where

$$\text{We}_l = \rho_g U^2 l / \sigma \quad (2.15)$$

Level ℓ	D/Δ	We_Δ	Oh_Δ
11	114	1.75	0.137
15	1820	0.11	0.55

TABLE 2. Characteristic numbers related to the grid size. The level ℓ is defined in Eq. (2.7).

MD level m	D/h_c	We_{h_c}	Oh_{h_c}
12	227	0.88	0.194
13	455	0.44	0.27

TABLE 3. Characteristic numbers based on the critical sheet thickness in our simulations. The manifold-death level m is defined in the text.

is the Weber number based on length scale l and Δ is the grid size. Similarly

$$Oh_l = \mu_l(\sigma\rho_l l)^{-1/2}$$

is the Ohnesorge number based on scale l . The values of We_Δ for two of the grids we use are given in Table 2. We also give the value of the Ohnesorge numbers Oh_Δ and Oh_{h_c} which characterize the interplay of viscous and surface tension effects. In particular they typify the regime of the Taylor-Culick rims (Song & Tryggvason 1999; Savva & Bush 2009) occurring at the edge of a sheet of thickness Δ or h_c . The Oh number of the thin sheets at the moment of hole formation is relatively large, implying a viscous Taylor-Culick flow and the absence of unsteady fragmentation as in Wang & Bourouiba (2018) and Kant *et al.* (2023).

The second important consequence of selecting the relatively small value $We_g = 200$ is that it makes the simulation sit on the boundary between membrane type and fiber type defined in Lasheras & Hopfinger (2000). Membrane-type in that later paper refers to the formation of bags and sheets. Thus the prevalence of thin sheets discussed in this paper may be less marked at higher Weber numbers, the sheets being replaced by fibers, and also less important at smaller Weber numbers where the flow may be less unstable.

3. Results

3.1. Uncontrolled perforation: numerical sheet breakup

Figure 3 shows a global view of the jet evolution (see also Movie1, Movie2, Movie3, Movie4, Movie5 and Supplementary Material. (for the prepublication, see <https://zenodo.org/doi/10.5281/zenodo.11110044>). The dynamics is initialized with a slightly penetrated jet at $t = 0$. At $t = 0.1$, a mushroom-like structure starts rolling up. The annular structure stretches and extends in the form of a ‘‘corona flap’’ that develops behind the mushroom head. A rim forms at the edge of this flap then detaches. It is visible at $t = 0.2$ as a corrugated and partially fragmented annular

ligament. As the jet evolves pulsation results in a periodic series of corona flaps seen at $t = 0.8$. These flaps interact with the ligaments coming from the mushroom head. At $t = 2$, the jet has evolved further and we can identify an interval in the core structure where the effect of pulsation is lost. Several mechanisms of droplet formation like sheet rupture, ligament breakup and their interactions with the jet core and corona flaps are seen. At $t = 3$, the jet is fully developed and we see long axial ligaments with a marked velocity gradient made visible by the color change along the axis, circular ligaments, corona fingers merging and sheet rupture. A large number of droplets and ligaments are produced in the mushroom tip region. Most of the phenomena illustrated above are also observed with controlled perforation, except the initiation of sheet rupture and annular ligament detachment.

Figure 4 shows a contrasting view of the jet with the camera direction aligned with the jet axis and the view positioned at the inlet. In Figure 4a the objects are colored by curvature, so small droplets are red and small bubbles, with negative curvature, are blue. The bubbles have been trapped in the bulk or core of the jet or inside other liquid masses. The likely mechanism for the formation of a bubble is liquid mass collision, for example droplet impact on the jet core. Many such droplet or ligament impacts are seen in Movie1. The surprising aspect of the detection is the relatively large number of droplets seen. In Figure 4b the objects are colored by axial velocity, as with Movie1 and Movie3. An interesting aspect of this view is to show the large dispersion in the axial velocities of the droplets.

We now discuss the statistical properties of the jet, in particular the droplet-size distribution in the case of uncontrolled sheet perforation or “no manifold death” case (no-MD case). As the jet advances, the droplet-size distribution evolves. This is shown in Figure 5. One can see that the droplet-size distribution has started to converge at $t = 1.8$ and is approximately converged at $t = 2.8$. The histogram thus only shifts in the vertical direction (the number of droplets), while maintaining the same qualitative nature. This histogram is bimodal with two peaks or local maxima. There is a large-amplitude peak corresponding to a smaller droplet size (referred to as peak 1) and a smaller-amplitude one corresponding to the larger droplet size (referred to as peak 2). We investigate the statistical convergence of the droplet size distribution by plotting in Figure 6 the histogram at $t = 3.5$ when the jet is fully developed. We plot various grid resolutions or levels on that same Figure. The highest resolution in the no-MD case corresponds to the Δ_{14} line. This implies $D/\Delta = 920$ grid points per initial diameter. Figure 6 has two important characteristics: (i) the histograms at various resolutions are qualitatively similar, that is bimodal with a major peak 1 at small scales and a minor peak 2 at large scales, and (ii) despite such high resolution, it is clear that there is no convergence for the droplet size distribution. However the tail region of the distribution, to the right of peak 2 shows some degree of convergence. In that tail region a Pareto distribution $n(d) \sim d^{-3}$ is seen reminiscent of such distributions found in other contexts (Balachandar *et al.* 2020; Pairetti *et al.* 2021).

The dependence of the two peaks with the grid size is shown explicitly in Figure 7b where we plot the ratios d_i/Δ_ℓ corresponding to the peaks as a function of the maximum level ℓ . We observe that the ratio for peak 1, d_1/Δ_ℓ remains constant around a value of 3, while for peak 2, d_2/Δ_ℓ weakly increases with ℓ . The grid dependence of these two peaks is synonymous with the absence of statistical convergence. We will discuss possible explanations for the behavior of these two peaks below, and in particular the relation between peak 1 and the curvature ripples appearing just before sheet rupture. Since this behavior is maintained at all resolutions, the constant scaling of the diameter d_1 of peak 1 with the grid size implies that no matter how much we refine the grid, since the

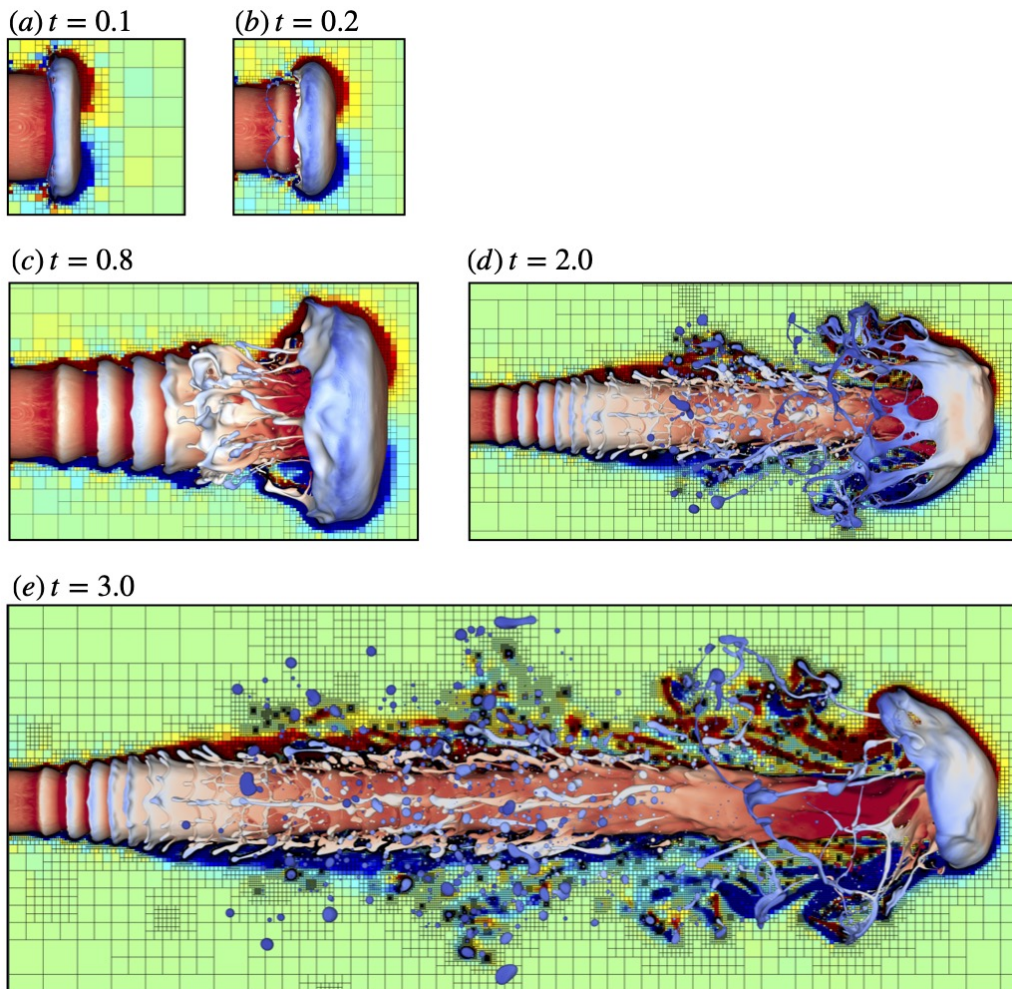


FIGURE 3. The advancing pulsed jet at various time instants t and level $\ell = 14$. The fluid interface is colored by the axial velocity and the background is colored by the vorticity. The background also shows the mesh refinement. (a) The pulsed jet develops a mushroom head and a rim. In (b) the rim detaches. (c) Development of flaps coming from the sinusoidal pulsation. (d) Jet entering in a regime where effect of pulsation is lost at the mushroom head. (e) A fully developed jet and a rich spectrum of droplets and ligaments. Since Re_g is rather low at 5800 there is relatively little vorticity away from the interface unlike in the case of Kant *et al.* (2023).

droplet diameter is scaling with the grid size $\sim 3\Delta$, the distribution of droplet sizes is grid-dependent.

The mechanism leading to peak 1 is related to the perforation of thin sheets. This perforation is observed to occur in two contrasted ways. A simple mechanism is the impact of small droplets on the liquid sheet. The droplets are formed by breakup previously occurring elsewhere in the simulation. The impacts yield in some cases the formation of an expanding hole, as shown on Figure 8. We note that such impacts have already been observed in previous studies such as those of Ménard *et al.* (2007) and Shinjo & Umemura (2010). Not all droplet impacts create perforations. In Figure 8, at time $t = 2.94$, we track the droplets indicated by arrows. We see that droplet impacts often create holes with a characteristic finger-like ligament inside the hole. Impacts are shown by arrows at time

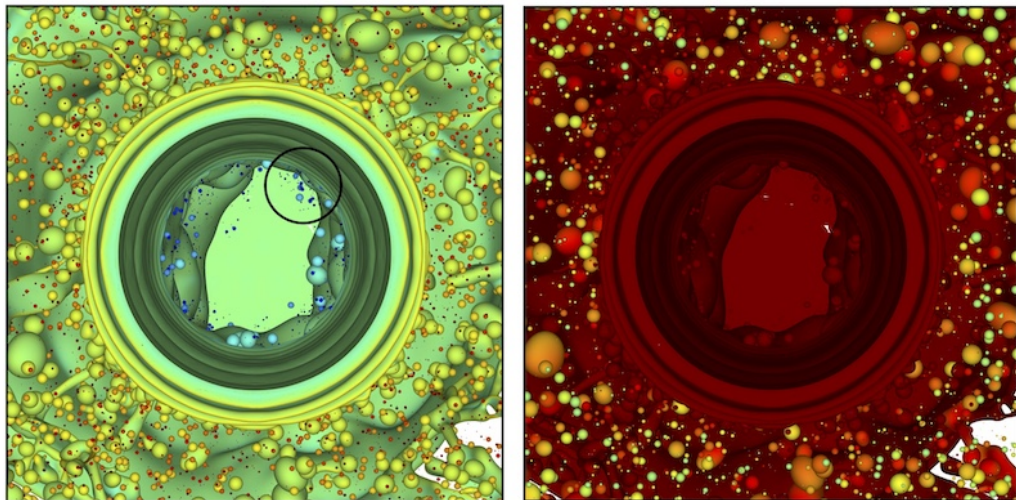


FIGURE 4. View from the inlet at time $t = 3.04$ showing the inner region of the central core liquid jet. Left image is colored by the curvature showing the encapsulation of gas bubbles identified by the negative curvature (blue) in the liquid core encircled in the black circle. The droplets have positive curvature (red). The entrained bubbles travel with the core jet velocity and could also result in the formation of a few compound droplets during atomisation or provide a physical breakup mechanism for thin sheets. The right image is the same as left one but colored by the axial velocity. The simulation corresponds to level $\ell = 14$ with manifold death method applied at level $m = 13$.

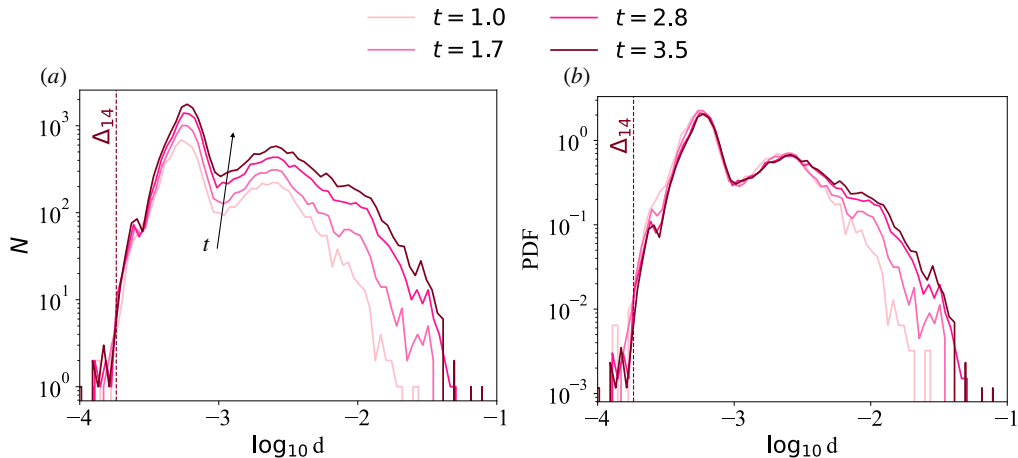


FIGURE 5. (a) The droplet-size number distribution and (b) the probability density function of the droplet diameter at various time instants. The plot shows that the PDF has converged in time $t \sim 2.5$. This time convergence determines the choice of the end time of the simulation at $t = 3.5$. Both (a) and (b) have 200 bins. The simulation corresponds to level 14 and the vertical dashed line represents the grid size.

$t = 3.10$ in Figure 8. In the lower panel at $t = 3.12$ and $t = 3.14$ some droplet impacts do not result in holes but that instead droplets merge with the sheet. This hypothesis was confirmed by repeated observations of the sheets at various angles and by visioning Movie4 and Movie5. The red arrow from $t = 3.14$ and $t = 3.16$ captures an interesting moment, where the droplet impact and sheet rupture happen simultaneously and it is

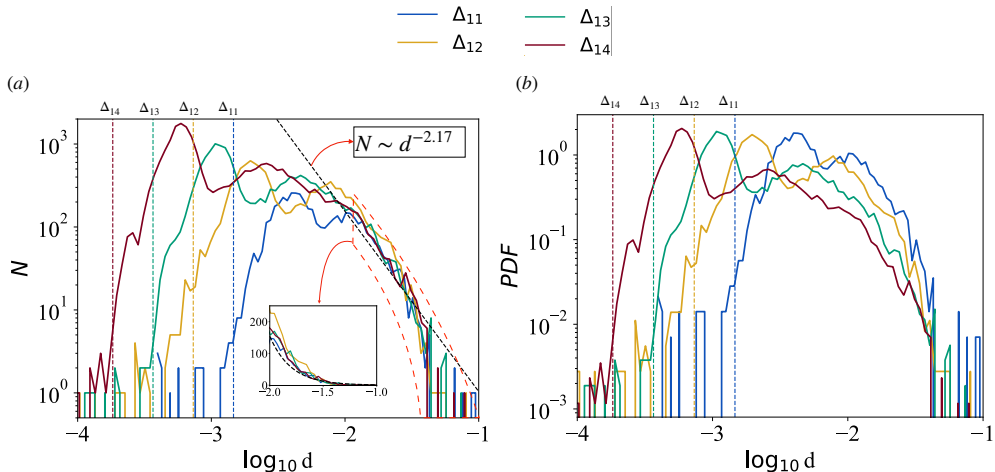


FIGURE 6. (a) The droplet-size distribution and (b) the probability density function of the droplet diameter d at the final time $t = 3.5$ for various grid resolutions. The grid sizes are shown with vertical dashed lines and Δ_ℓ is defined as in (2.7). The inset in (a) shows the converged tail region. All the plots are done with 200 bins.

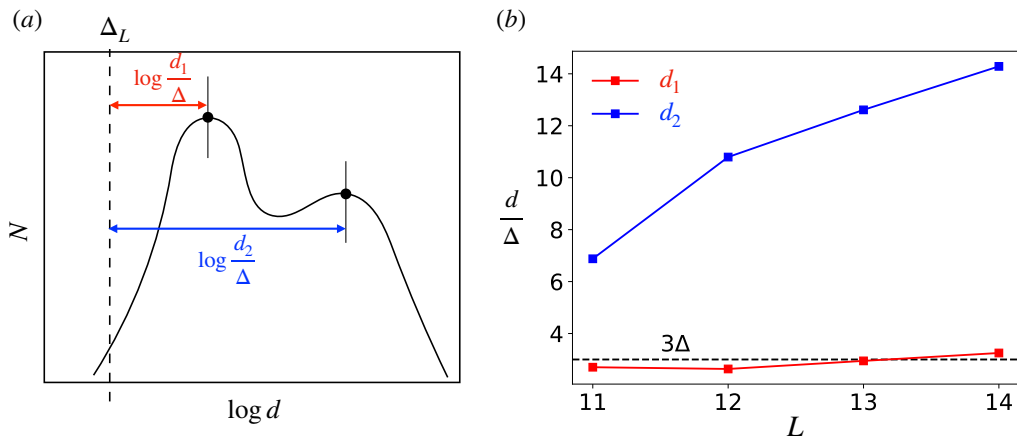


FIGURE 7. (a) Schematic of the bimodal droplet size distribution. The arrows indicate the logarithmic distance from the grid size $\log d_i/\Delta = \log d_i - \log \Delta$. (b) The values of d_i/Δ as a function of the maximum grid refinement level ℓ for the distribution of Figure 6. The dashed line is at 3Δ implying the droplets at peak 1 have a grid dependent diameter of $d_1 \sim 3\Delta$.

unclear if the hole was created by the numerical rupture process discussed below or by droplet impact.

Another mode of thin sheet perforation, much more complex and purely numerical, is illustrated on Figure 9 as well as Movie4 and Movie5. The curvature coloring of the interface helps us identify the perforation spots. We see high frequency oscillations of the curvature field in form of alternating red and blue colors. These indicate the ripples originating at the fluid interface before the sheet rupture happens. Finally, at $t = 2.82$, we see a dense network of small-diameter ligaments, scaling with grid size. Another mechanism that may contribute to peaks 1 and 2 is the rupture of ligaments, also shown on Figure 9. Small diameter ligaments have large curvature and are thus easily identified

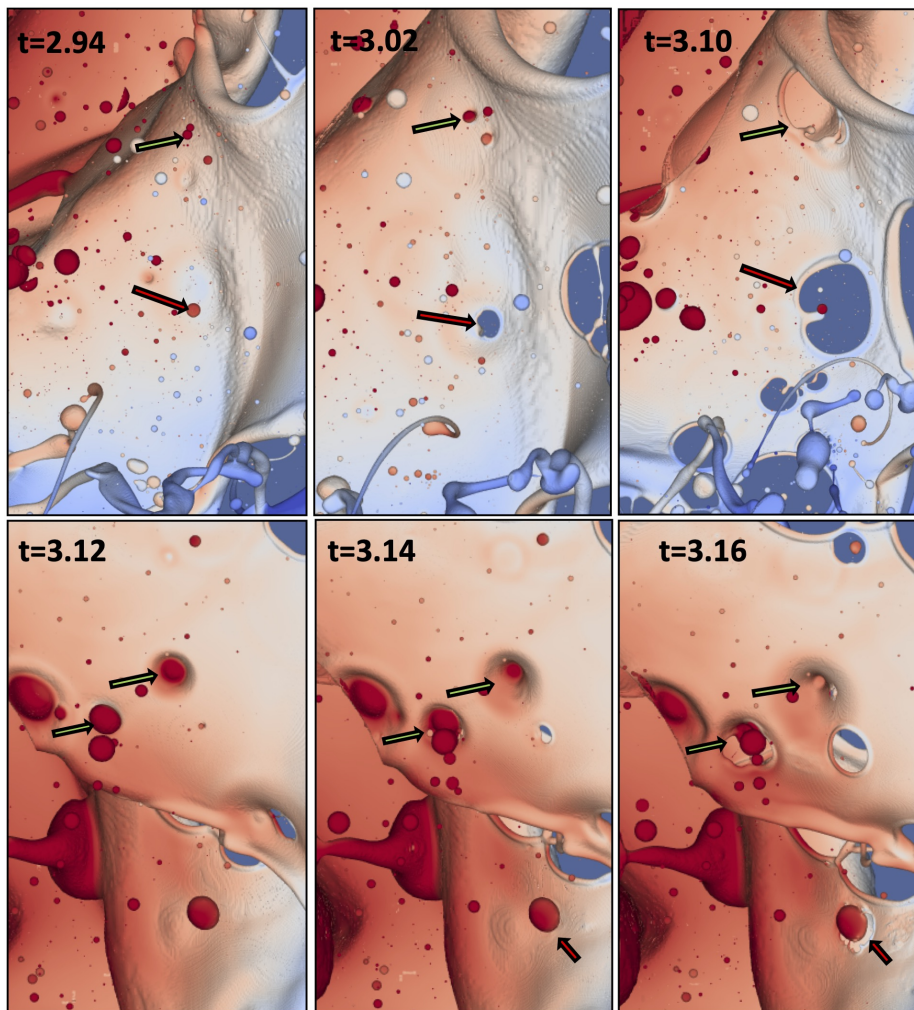


FIGURE 8. Droplet impacts on the frontal liquid sheet. The points of interest are indicated by the arrows. Droplet impacts can result in holes with characteristic ligaments as seen at $t = 3.10$. In some cases droplets coalesce into the sheet seen at $t = 3.12$ and $t = 3.14$. At $t = 3.16$, the sheet is ruptured but the droplet is still identifiable. All simulations are for maximum level $\ell = 13$. The manifold death method is not applied. The interface is colored by axial velocity. The artefacts or corrugated surfaces particularly visible at $t=3.02$ and $t=3.10$ at the top right are not aliasing artefacts (due to an approximate isosurface interpolation) but are representative of the curvature oscillations seen in the next figures.

by their color. They break physically and not numerically by the Rayleigh-Plateau instability. The origin of these ligaments themselves is often an expanding hole whose rim collides into other rims. To investigate the small-scale ligament networks, we zoom around such a breakup event in Figure 10. We see that a weak spot develops and curvature ripples appear at $t = 2.78$ as soon as the sheet reaches a thickness a few times the cell size as shown in the inset. These curvature ripples then give rise to ligament networks inside the expanded hole eventually leading to the grid-dependent droplets. To summarise, as the sheet reaches a thickness of order 3Δ , the rupture chronology is as follows: *thin sheet regions* > *curvature ripples* > *ligament networks* > *tiny droplets* ($d \sim 3\Delta$). Since this

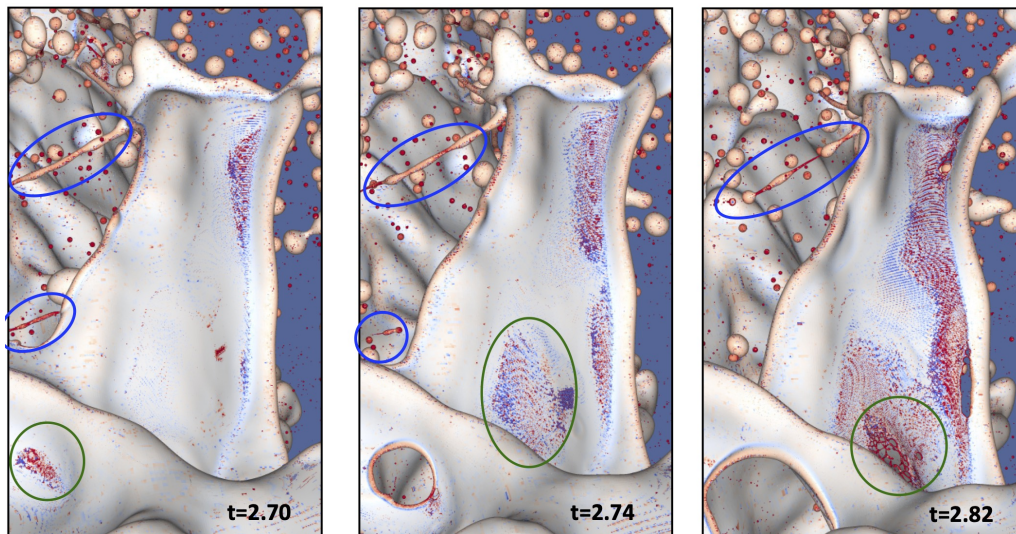


FIGURE 9. Appearance and evolution of the curvature ripples on the interface. The interface is colored by the interface curvature. These ligaments are colored a darker red and the interfaces on the thin sheets are closer to white. Ligament rupture is encircled in blue. The rupture or ligament pinch off appears in a darker red color. Sheet rupture, encircled in green, displays curvature ripples in the form of red-blue oscillations. At time $t = 2.82$, the green-circled rupture region displays a grid-dependent ligament network that has evolved from these ripples. These images correspond to a level $\ell = 14$ simulation. (See also Movie4 and Movie5.)

sequence of events is inherent to the numerical breakup of thin sheets, it is impossible to escape its occurrence by increasing the grid refinement, although refinement can delay it. The numerical sheet breakup identified here is the direct cause of the lack of convergence of peak 1. Indirectly, the formation of droplets and ligaments of a given size in a non-converged manner leads to all the droplet size counts to be unconverged as these other size droplets are formed through coalescence and breakup events from the peak 1 droplets and similarly scaled ligaments.

3.2. Controlled perforation by the manifold death method

We now present the results of atomization when we apply the manifold death method. Here we adopt the following conventions.

(i) The octree maximum refinement level ℓ defines finest grid size as given in Equation (2.7).

(ii) The manifold death level m implies that the critical thickness for punching holes is given by $h_c = 3\Delta_m$.

As an example, the notation $(\ell, m) = (13, 12)$ would mean that the finest cell size in the simulation is Δ_{13} and the critical thickness at which holes are being punched is $h_c = 3\Delta_{12} = 3 \times (2\Delta_{13}) = 6\Delta_{13}$. This convention for the definition of the “manifold death level m ” maintains consistency with the comments in the code <http://basilisk.fr/sandbox/lchirco/signature.h>. The extent of the integrated region in the quadratic form computation leads to the correspondence $h_c = 3\Delta_m$.

The overall evolution of the jet shows important variations with the no-MD case. Comparing Figure 11 to Figure 10 i) the mist of very small droplets near the mushroom head has disappeared ii) the mushroom-head corona-flap sheet is more affected by holes and breakups and iii) the dark blue droplets at mid-length are of smaller size in the MD

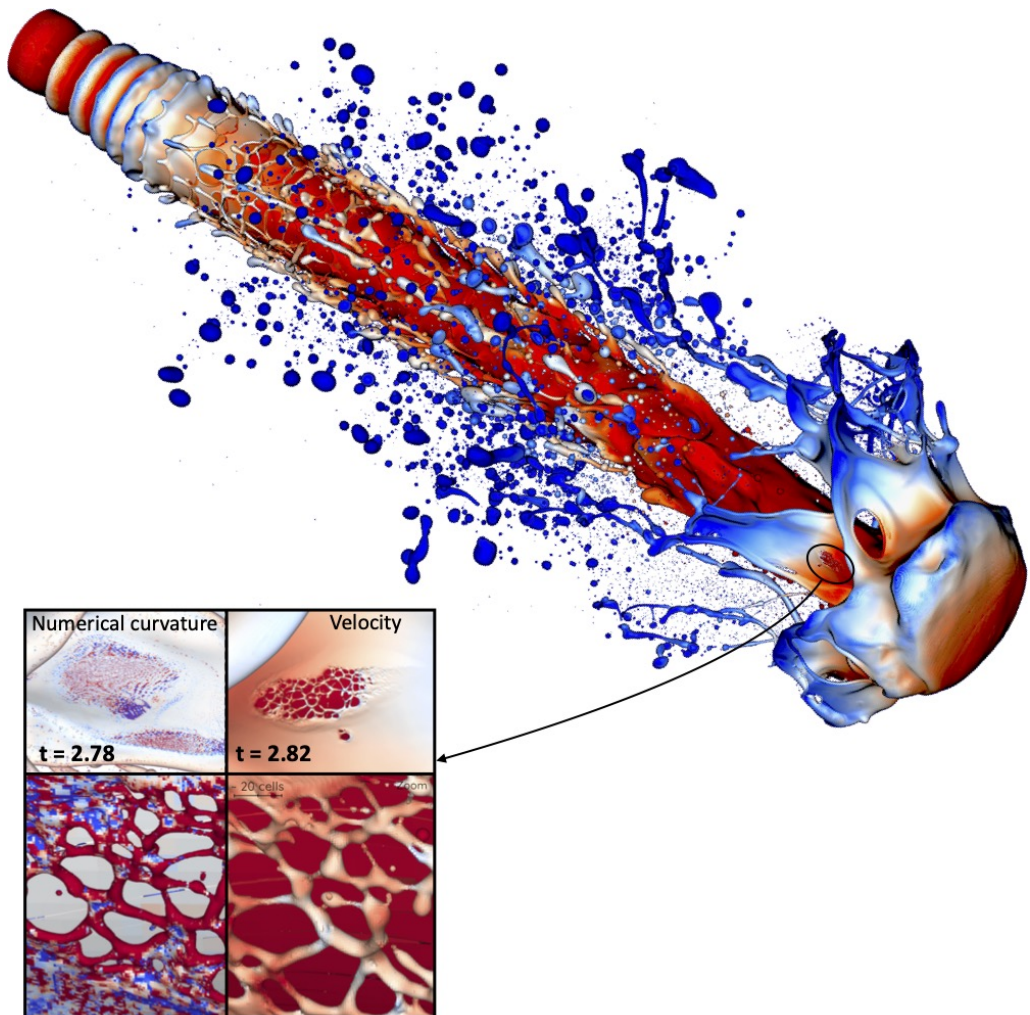


FIGURE 10. The fully-developed jet at $t = 2.8$. The inset shows a zoom-in at the sheet rupture spot showing the curvature ripples in the weak spot about to be punctured and the resulting ligament network. This ligament network eventually produces grid-dependent droplets. The simulation shown here is at level $\ell = 14$.

case of the current figure. This last fact can also be seen in Figure 13 where one can see that the peak of droplets near $\log_{10} d = -2$ for the no-MD case (black curve) has been shifted to smaller droplets in the MD case (red curve).

Figure 12 shows the evolution of the probability density function of the droplet size distribution with time. Similar to the no-MD plots, we see that here also the statistics are converged in time as soon as $t = 2.5$. When compared to Figure 6, we see that the peak corresponding to the smaller droplet size has a smaller amplitude. At this point in the exposition it may be useful to recall the connection between the number distribution and the probability density function (PDF). We consider a fixed instant of time t_0 . We partition the interval of droplet sizes $(0, d_M)$ into a discrete set of M intervals $[d_i, d_{i+1} = d_i + \delta_i)$. The index i varies from 0 to i_m . The number of droplets with diameter in the interval $[d_i, d_i + \delta_i)$ is $n_{d,i}\delta_i$. The probability density function $p(d)$ is proportional

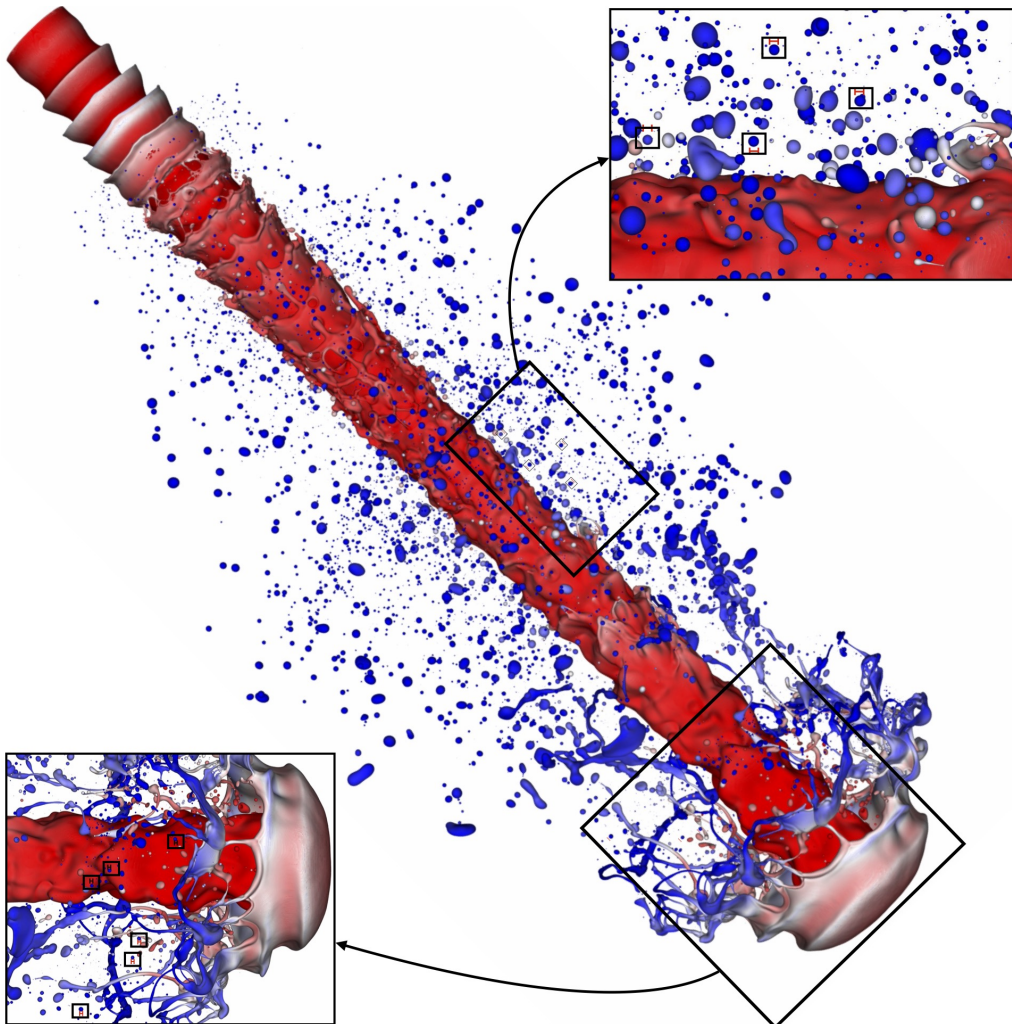


FIGURE 11. The jet at $t = 3.1$ at level $\ell = 14$ with Manifold Death (MD) applied. The MD level is 13. Comparing with the no-MD Figure 10 several qualitative changes are seen. An important one is that the tick blue droplets (blue means negative axial velocity) are definitely smaller in this MD case. The insets and the boxes indicate droplets that are near the maximum size of the distribution in the converged region.

to the expected value $\langle n_{d,i} \rangle$ as follows

$$p(d_i) = \frac{1}{\mathcal{N}} \langle n_{d,i} \rangle,$$

where the normalising factor is

$$\mathcal{N} = \sum_{i=0}^M \langle n_{d,i} \rangle \delta_i.$$

We are plotting the number frequency of droplet counts $n_d(d, t) = \langle n_{d,i} \rangle$ instead of the PDF $p(d, t)$. The pulsed jet process is both deterministic and transient, so the value of $n_{d,i}$ obtained at $t = t_0$ in a simulation is well defined. The expected value $\langle n_{d,i} \rangle$ differs very little from the numerically obtained value $n_{d,i}$. Moreover in such

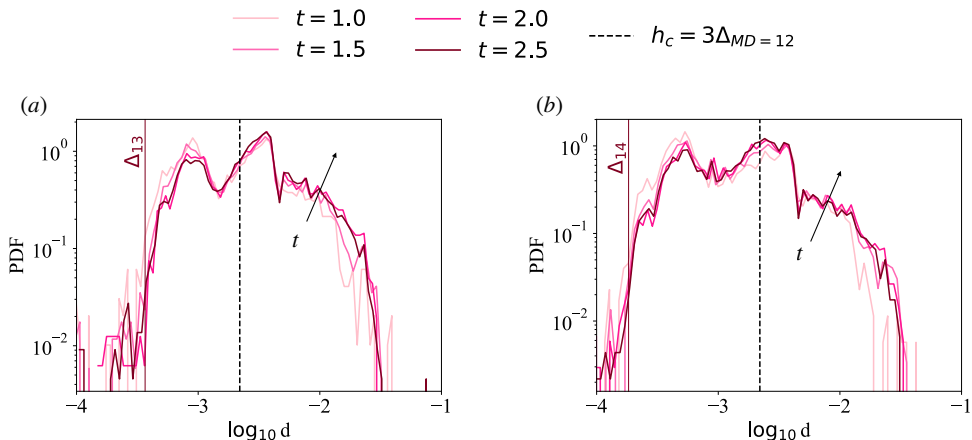


FIGURE 12. The probability density function at various times t for the droplet size distribution when manifold death is applied. The PDF has converged in time at $t = 2.5$. (a) PDF at maximum level $\ell = 13$ and MD level $m = 12$ and (b) the PDF at maximum level $\ell = 14$ and MD level $m = 12$. The critical hole punching thickness $h_c = 3\Delta_{m=12}$ is shown as the black dashed line and is the same for both plots.

a deterministic process no difference is expected between two realizations, that is two identical simulations should yield identical droplet counts. On the other hand in a jet with a random upstream injection condition instead of a pulsed injection condition, the simulation is not deterministic and the value of $n_{d,i}$ obtained in a simulation at some time t is fluctuating. The transient nature of the jet is also important. In a steady state simulation (which should be obtained some time after the jet starts flowing out of the simulation domain) initial perturbations are amplified chaotically and the system is again probabilistic. Thus our pulsating initial condition simplifies somewhat the analysis by yielding a deterministic instead of a probabilistic number density.

We show the number density $n(d)$ in Figure 13. Figure 13a shows the histograms at various grid resolutions for a fixed manifold death threshold $h_c = 3\Delta_{12}$. The distribution is again bimodal, but the peak corresponding to the smaller droplets is weaker. We also observe a clear converged region in the interval $[d_c, d_{i_{m+1}})$, where d_c is the minimum converged equivalent droplet diameter or “converged diameter” for simplicity. The extent of the converged region increases, that is d_c decreases as the grid size Δ_l decreases. In Figure 13a the vertical line marks d_c for two consecutive grid sizes. We have shaded the onset of the non-converged region between two consecutive grid refinements for clarity.

In practice the “converged diameter” d_c is determined from the comparison of a pair of distributions from simulations of two different grid sizes Δ_l . We note this pair $\{\Delta_{l_1} - \Delta_{l_2}\}$. In Figure 13a the orange vertical line marks d_c for the pair $\{\Delta_{14} - \Delta_{13}\}$. Similarly, the purple vertical line marks d_c for the pair $\{\Delta_{15} - \Delta_{14}\}$. Some additional information may be obtained by investigating a no-MD case. In such a case, there is a typical sheet thickness at breakup h_e that is comparable to the controlled breakup for $h_c \simeq h_e$. Indeed the critical breakup film thickness h_e for no-MD is $h_e \simeq 1.5\Delta$. Then the above case $h_c = 3\Delta_{12}$ with manifold death has a critical sheet thickness equal to, per expression (2.7) to $h_e = 1.5\Delta_{11}$ in the no-MD case at level 11. Thus the no-MD simulation at $\ell = 11$ is a rough equivalent to the three simulations with MD level $m = 12$. The vertical black line is the converged thickness d_c for the pair $\{\Delta_{13}, \Delta_{11}\}$ where the first simulation is MD and the second is no-MD. One sees on Figure 13a that the converged diameters, indicated by the solid vertical lines decrease and tend to approach the critical sheet thickness h_c

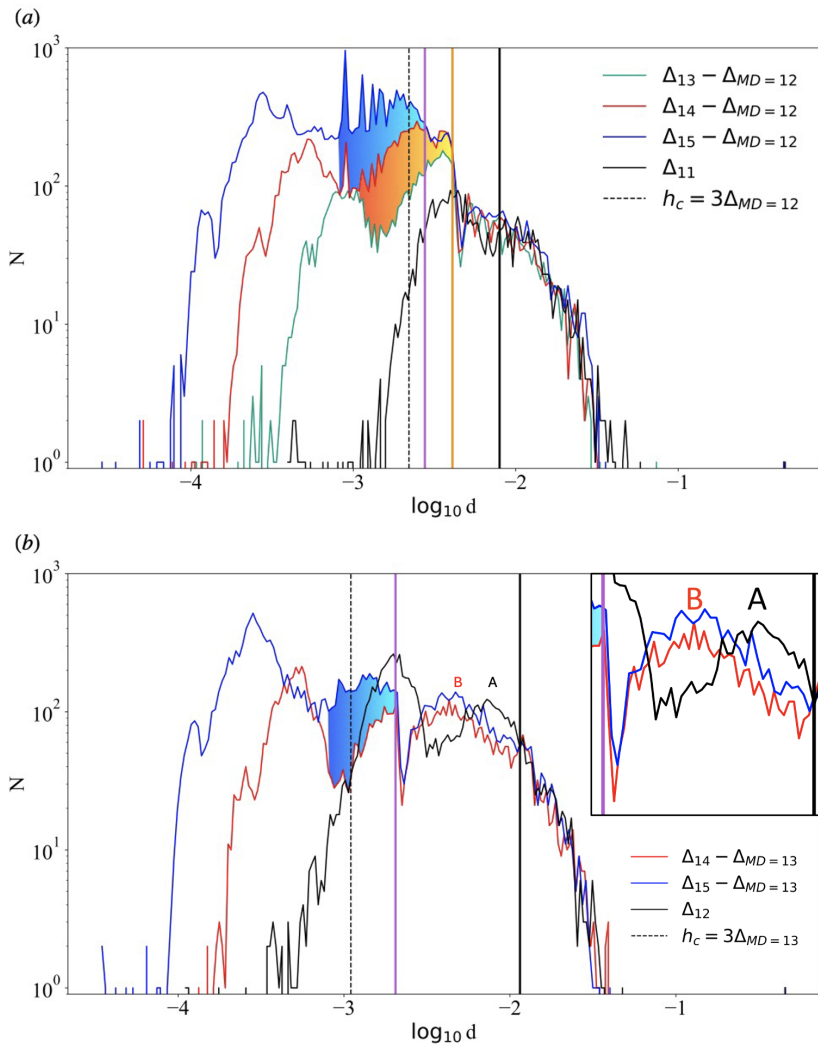


FIGURE 13. The droplet size distribution at various resolutions with the manifold death method applied. The curves with legend $\Delta_\ell - \Delta_{MD}=m$ imply that basilisk level is ℓ and the MD level is m . The dashed black vertical line represents $h_c = 3\Delta_m$, that is the critical thickness of punching holes. The solid vertical lines correspond to the values of the converged diameter d_c . This diameter marks the smallest diameter above which the number distribution is converged (see the main text). All curves in (a) have fixed $h_c = 3\Delta_{12}$ and all curves in (b) have fixed $h_c = 3\Delta_{13}$. Note that the Δ_{11} curve in (a) and the Δ_{12} curve in (b) indicate the no-MD method and roughly correspond to respectively $h_c = 3\Delta_{MD=12}$ and $h_c = 3\Delta_{MD=13}$ due to implicit VOF breakup. The shading is done to emphasize the departure from the converged region. We see that d_c approaches h_c as the grid size is reduced. The inset shows the important change in the typical sizes of droplets in the first peak above h_c as MD is applied. Peak A corresponds to peak 2 in the no-MD distributions of Figure 6 while peak B, with much smaller droplets, to droplets seen in the MD Figure 11.

for MD breakup, represented by the dashed vertical line. We now show the droplet size distribution and converged region for a smaller critical sheet thickness $h_c = 3\Delta_{13}$. In Figure 13b we see similar results but with only two instead of three levels $l = 14$ and 15. Since a simulation at Δ_{15} is already quite expensive (it implies an equivalent of 35

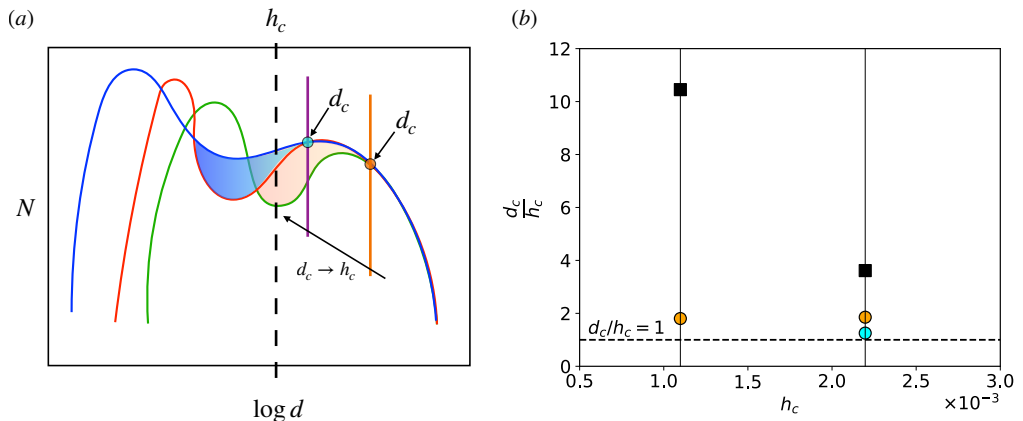


FIGURE 14. (a) Schematic of the comparison of two simulations and how it allows to define the “converged diameter” d_c . It is seen that d_c approaches h_c as the simulations are refined. (b) Plot of d_c/h_c versus h_c corresponding to the d_c values of Figure 13. Along a fixed h_c , the d_c/h_c points move closer to unity as the maximum level is increased. The black squares corresponds to the No MD case while all circles are for the cases with MD.

trillion cells for a uniform grid with Δ_{15}), we did not perform a third simulation at $l = 16$ in that case. A zoomed-in view for the converged region d_c for each consecutive pair is shown in Appendix E.

The variation of the converged diameter d_c as a function of h_c and Δ_ℓ is shown explicitly in Figure 14. Figure 14a illustrates schematically how the converged diameter approaches h_c as Δ_ℓ is reduced. Figure 14b shows the data in the $d_c/h_c, h_c$ plane. Each data point in that plane corresponds to a simulation pair discussed above such as $\{\Delta_{14} - \Delta_{13}\}$, and to a vertical line in Figure 13. Following a vertical line in Figure 14b, one can see d_c tending to h_c as the grid is refined for a fixed h_c .

Figure 15 shows a zoom-in at a hole expansion that was initiated by the manifold death method. The phase modification region is a cube but in less than 5-10 timesteps the hole takes a rounded shape due to surface tension and starts expanding. When these holes expand, we do not see the noisy curvature ripples that resulted in grid-dependent droplets in the no-MD simulation of Figure 10. This qualitative improvement in sheet collapse helps to obtain grid convergence.

The manifold death procedure we use is tuned to a relatively large frequency of hole formation. This results in features such as those shown in Figure 16. We see that once we detect a thin sheet and the MD process generates holes, these expand. However, it often happens that before the holes have expanded over the entire sheet more holes are punched just outside the rim. These kind of holes are identified in black circles in Figure 16. Experimental photographs and the reasoning in Appendix A point to a smaller number of holes. This smaller number could be achieved by an improved MD algorithm that would involve a more realistic model of the physical process of hole formation.

The final result of our manifold-death-enhanced study of droplet sizes is summarized on Figure 17. In this Figure we select two distributions of droplet sizes at two MD levels, $m = 12$ and $m = 13$ and we keep the ratio of the grid size to the MD threshold h_c/Δ_ℓ constant so the level difference is always $\ell - m = 2$. The two obtained distributions are similar to each other, with a sudden increase in droplet number at the edge of the converged region.

Moreover, these plots show that a sufficiently thin grid produces a bump-shaped

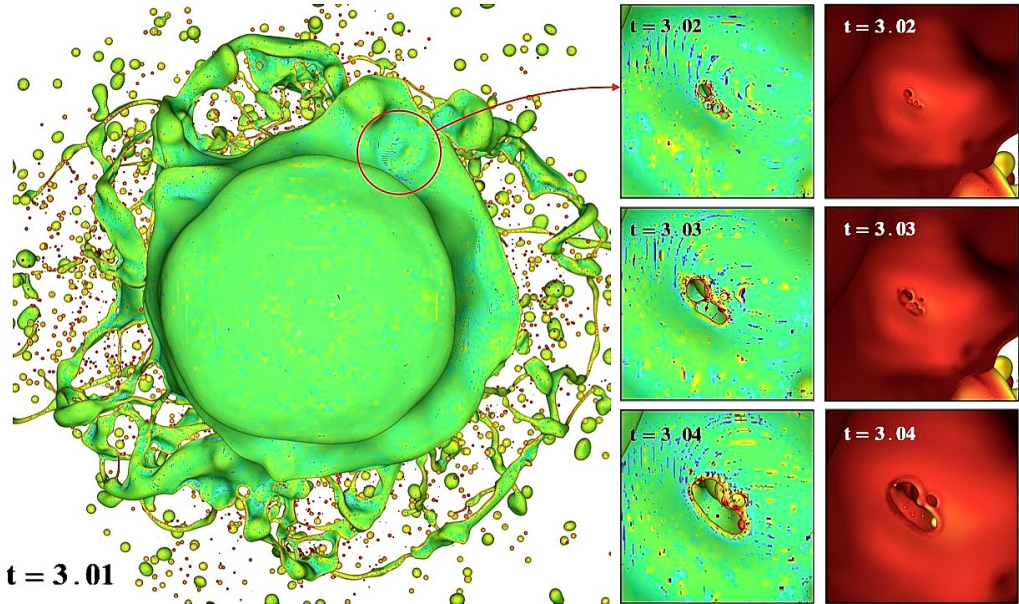


FIGURE 15. Sheet perforation when the manifold death method is applied. Unlike Figure 10, the holes do not contain large regions containing curvature ripples. Holes are punched at $t = 3.01$ and expand with time as shown. The interface in the left part is colored by curvature and on the right is colored by the axial velocity. The simulation shown here corresponds to $(\ell, m) = (14, 13)$

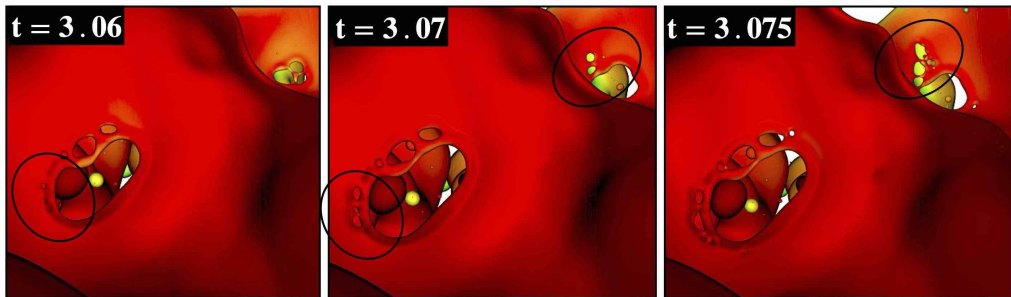


FIGURE 16. Further evolution of the holes of Figure 15. The image is colored by axial velocity. We see that near the rims of the main expanding holes, additional holes are punched, encircled in black. (Manifold death is applied.)

distribution with a clear maximum (this is the case at $m = 13$ but not at $m = 12$). This maximum is located at $d_{\max}/D = 4.3 \cdot 10^{-2}$ in our case. It is interesting to try to understand the origin of this bump. By dimensional analysis the maximum should be expressed as

$$d_{\max} = Df(h_c/D, N_1, \dots, N_n). \quad (3.1)$$

where N_i are the dimensionless numbers of the problem other than h_c/D . It is quite tempting to assume that in some range of h_c/D and of the dimensionless numbers a proportionality relation holds. From the existing data it would be

$$d_{\max} = 4.3 h_c. \quad (3.2)$$

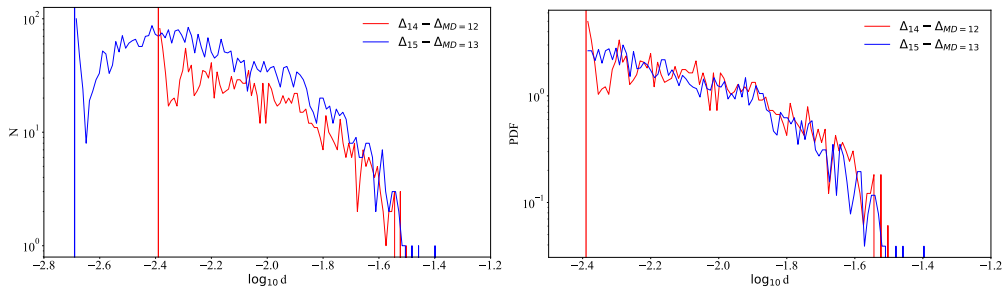


FIGURE 17. Two distributions of droplet sizes at two MD levels, $m = 12$ and $m = 13$, with the same ratio of the grid size to the MD threshold h_c/Δ_ℓ . We only plot the converged region, that is $d > d_c(h_c)$. The most refined simulation $(l, m) = (15, 13)$ yields a distribution somewhat but not exactly similar to the less refined. Both distributions show a sudden increase in droplet number (a “ridge”) as the droplet size is decreased at the edge of the converged region. The vertical line shows the limit of convergence d_c . The left plot shows the un-rescaled number distribution, while the right plot shows the PDFs. The right plot is clipped to show the PDFs $p(d)$ for $d > d_c(m = 12)$, where d_c is the edge of the converged region for $m = 12$.

We finally note that this is to our knowledge the only example of a converged bump-shaped (unimodal) distribution in simulations of jet atomization at large Weber number.

4. Conclusions

We have studied an atomizing, pulsed round jet at a succession of grid sizes with unprecedented resolution. Visual inspection of the resulting interface topology reveals a new numerical phenomenon preceding hole formation in the VOF method: high frequency curvature oscillations followed by the appearance of a small-scale network of ligaments. The inspection of droplet size frequency distributions reveals the presence of two large peaks tied to the grid size. It is clear that the small- d peak and probably the second one are related to the unphysical breakup. Although convergence of the distribution of droplet sizes is not achieved in the whole range, a partial convergence is observed at large scales. We thus recover the convergence properties observed in another context by Chirco *et al.* (2022) and by Tang *et al.* (2023).

To mitigate this effect we apply the manifold-death procedure of Chirco *et al.* (2022). The procedure forces hole formation when sheets reach a set thickness h_c . Number frequency plots show convergence in a range of droplet sizes starting at a critical diameter d_c . The extent of this converged range increases when either the grid size Δ_ℓ or the critical thickness h_c are decreased. For a fixed h_c , when we reduce Δ_ℓ , the converged diameter d_c approaches the critical thickness h_c . We thus recover the convergence properties observed by Chirco *et al.* (2022) and by Tang *et al.* (2023). We characterize them in the h_c - d_c plot of Figure 14b. We note that the statistical accuracy is much stronger in the present case since our pulsed jet produces three orders of magnitude more droplets than the phase inversion case of Chirco *et al.* (2022). We do not have a definite explanation for the lack of convergence below the diameter h_c , that is we are not sure why d_c does not decrease below h_c as Δ_ℓ is decreased. We can however offer several avenues for future exploration. One is the smoothness of the manifold death procedure itself and the choice of its parameters such as the number of holes punched or the punching frequency $1/\tau_m$. For the first time in VOF simulations of atomization, a bump-shaped, converged droplet size distribution is obtained. Even without convergence, bump shaped distributions are harder to obtain in VOF simulations than in Level-Set or Diffuse-Interface simulations

where they are common Herrmann (2010); Khanwale *et al.* (2022); Saurabh *et al.* (2023) because these two other methods tend to “evaporate” small droplets, as shown on Figure 1. A scaling relation for the position of the bump is suggested. The bump only appears at the highest level. Whether the proposed scaling (3.2) for the bump would persist if yet more refined simulations are performed is an interesting open question.

Beyond the physics of hole formation and expansion, the simulations reveal a rich spectrum of elementary phenomena that are the building blocks of atomization. These include networks of well resolved ligaments in and around holes, ligaments detached from the main liquid core and either aligned or at an angle with it, bubbles trapped in liquid regions, droplets impacting on sheets etc. This rich physics is seen in increasing detail as grid resolution is increased. For example, the sharpness and apparent realism of the various expanding holes, with attached ligaments or networks of ligaments inside, was not seen in previous simulations, for example in Ling *et al.* (2017). Moreover a large number of each type of object or “building block” is visible at each instant of time, leading to more significant and converged statistics.

A tantalizing question is that of the physical, as opposed to numerical, origin of the perforations. We attempt some discussion of this issue in Appendix A. Two types of rate processes for heterogeneous nucleation are postulated, one based on in-sheet germs or nuclei, such as small bubbles, the other on external perturbations such as floating droplets or particles. Our simulations do not allow to decide at present between these two processes for hole formation. However they may in the future help understand how to discriminate between them. Moreover, the presence of a large number of bubbles in the jet core shown in Figure 4 shows one possible origin of the distribution of bubbles in liquids. Interestingly, in some atomisation experiments such as the one of Grenoble (Matas *et al.* 2011) the previously atomised water is recycled into the atomising liquid sheet which is then more bubble-rich.

Unlike most of the other round jet simulations in the literature, ours is bimodal and even trimodal after the application of manifold death. It seems that a mode emerges from the best resolved MD simulations, indicating that the appearance of a maximum of droplet size well in the converged region is possible only if the physics is correctly captured down to scales much smaller than the integral scales such as the jet diameter D .

Another important characteristic of simulations and experiments are the state of the fluids at the inlet. The primary mixing-layer instability in our simulations is initiated not by upstream turbulence as in most round jet simulations in the literature but by a pulsating flow. As far as we could see by comparing the visual aspect of the fragmenting interface as well as comparing the obtained number distributions and PDFs, we do not see marked qualitative differences with simulations without noisy or turbulent inflow conditions.

The perspectives opened by this work are numerous. Clearly, simulations of comparable quality at higher Weber number may allow investigation of the “fiber-type” regime observed in many experiments. Currently our simulations sit on the boundary between membrane type and fiber type. Simulations of comparable resolution should also be performed in the planar mixing-layer case investigated experimentally by the Grenoble group (Ben Rayana *et al.* 2006; Fuster *et al.* 2013) and numerically by Jiang & Ling (2021). The latter authors performed very high resolution simulations with hole formation, and interestingly obtained a bimodal distribution, but they did not apply a controlled perforation scheme as in this paper. Simulations of secondary atomization, that is the atomization of a droplet suddenly plunged in a high speed flow has already been performed together with controlled perforation by Tang *et al.* (2023) achieving

convergence of the PDF. The secondary atomization case is probably the most promising for an eventual comparison of the distribution of droplet sizes obtained by simulation with the rich experimental data reviewed and modelled for example by Jackiw & Ashgriz (2022).

More distant perspectives, or more difficult problems remaining to solve are in our opinion twofold. One is clearly the improvement of the manifold death procedure, to have a better control of the number of holes punched in each thin sheet region, and a smoother manner to “cut-out” the initial hole. Another challenging future task is to use this type of simulation to infer, by careful matching of simulation results and experiments, the physical roots for weak spots and sheet perforations. Given the wide variety of mechanisms that have been advanced, this is a formidable enterprise for which we hope this paper could provide partial guidance.

Acknowledgements

We thank Marco Crialesi and Daniel Fuster for fruitful discussions. This project has received funding from the European Research Council (ERC) under the European Union’s Horizon 2020 research and innovation programme (grant agreement nr 883849). We thank the European PRACE group, the Swiss supercomputing agency CSCS, the French national GENCI supercomputing agency and the relevant supercomputer centers for their grants of CPU time on massively parallel machines, and their teams for assistance and the use of Irene-Rome at TGCC and ADASTRA at CINES.

Declaration of Interests

The authors report no conflict of interest.

Appendix A. A phenomenological theory for hole nucleation and expansion

Independently of the physical mechanism for hole nucleation, and only on the basis of a model where the nucleation probability increases as the sheet $h(t)$ decreases it is possible to predict the effective number of holes that will be observed. First consider the typical size $L(t)$ of an expanding bag. Experimental observations (Kant *et al.* 2023; Opfer *et al.* 2014) show that bags inflate exponentially. We consider only large scale bags governed by the large scale properties of the flow that thus inflate at a rate $\omega = 1/\tau_c$. Then $L(t) \sim L_0 \exp(\omega t)$ and the bag thickness decreases as $h(t) \sim h_0 \exp(-2\omega t)$. Theory and experimental observations (Villermaux & Bossa 2009; Opfer *et al.* 2014; Marcotte & Zaleski 2019; Kant *et al.* 2023) indicate the scaling

$$\tau_c = \frac{D}{U} \left(\frac{\rho_l}{\rho_g} \right)^{1/2}. \quad (\text{A } 1)$$

Once weak spots are activated in such a bag they expand at the Taylor-Culick velocity (Taylor 1959; Culick 1960)

$$V_T = \left(\frac{2\sigma}{\rho_l h_c} \right)^{1/2}. \quad (\text{A } 2)$$

If N holes are activated in a typical bag of size L , the average distance between hole nuclei positions scales like $\lambda = LN^{-1/2}$. This distance is covered by the expanding hole

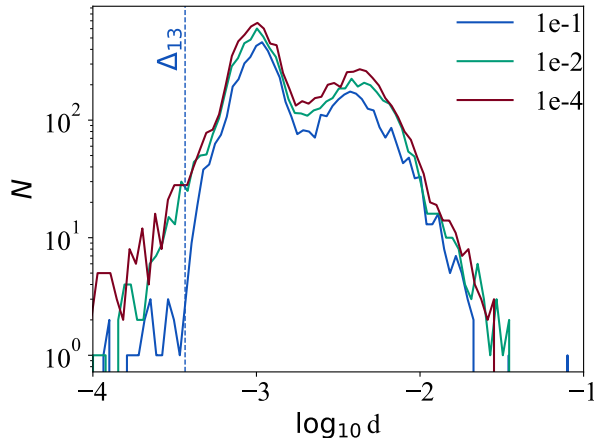


FIGURE 18. The droplet size frequency for maximum level $\ell = 13$ and no manifold death at various error thresholds for the velocity.

edges in a time $\tau_1 = \lambda/V_T$ and

$$\tau_1(N, h) = LN^{-1/2} \left(\frac{2\sigma}{\rho h} \right)^{-1/2}. \quad (\text{A } 3)$$

We now distinguish between two extreme cases. In the first case $\tau_1(1, h_c) \ll \tau_c$. This means that after the first hole has formed, it will expand to the whole bag size before the sheet has significantly thinned. Another way of expressing this is to say that the hole expansion time is much shorter than the sheet thinning time.

In the other extreme case, the hole expansion time for a single hole is much longer than the sheet thinning time. It is then likely that many more holes shall nucleate. One then needs to consider the expansion time $\tau_1(N)$ for a large number of holes N . We now borrow an argument from the theory of bifurcations or instabilities in time-varying environments. The Kibble-Zurek theory (Kibble 1976; Zurek 1985) argues that the time scale of the environment variation is equal to the time scale of the growth of the instability. We accordingly posit that the multi-hole expansion time $\tau_1(N)$ scales like the characteristic bag expansion time τ_c that is

$$\tau_1(N) = \tau_c. \quad (\text{A } 4)$$

Then from the balance of time scales (A 4) the number of holes in a bag of size L can be obtained as

$$N_1(h_c) \sim \frac{h_c \rho_g L^2 U^2}{D^2 \sigma} = \frac{h_c}{D} \text{We}_g. \quad (\text{A } 5)$$

There is a degree of uncertainty for the ratio L/D , however L and D are both integral scales of the turbulent flow and can be considered of the same order of magnitude. (We disregard the possible case where eddies of smaller scale than the integral scale of turbulence are sufficiently energetic to generate smaller scale bags.) The number of holes per bag in this mechanism is then the ratio of two typically large numbers, D/h_c and We_g . Equation (A 5) is valid in the second extreme case when the right hand side is much larger than unity. A very rough extrapolation between the two extreme cases is then

$$N(h_c) \sim \text{Max}[1, N_1(h_c)]. \quad (\text{A } 6)$$

In most cases one expects L to be of the same order of magnitude as D which leads to

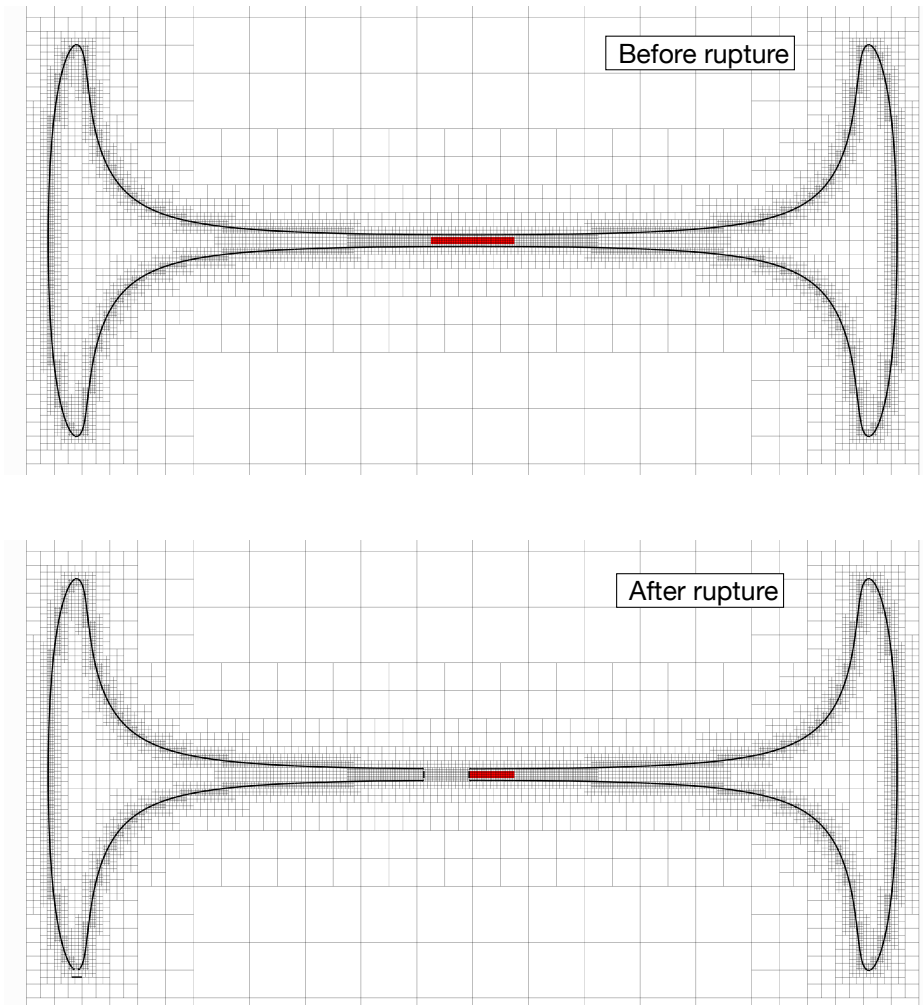


FIGURE 19. Thin structure detection and manifold death perforation in an example 2D case. The cells tagged as thin structure at the MD level are filled by red color. The upper image corresponds to the fluid structure right before perforation when a thin sheet is detected and the lower part shows the fluid structure after perforation. Note that the images are at same timestamp to explicitly show the perforation process. The image is done for case $(\ell, m) = (9, 8)$. Adaptive mesh refinement can be seen in background.

the simplified prediction

$$N_1(h_c) = We_{h_c}. \quad (\text{A } 7)$$

Table 2 gives some typical values for We_{h_c} and We_{Δ} , allowing a prediction of the expected number of holes in the corresponding simulations.

Appendix B. Grid adaptation

As discussed in the main text, the mesh is adapted dynamically, by splitting the parent cells whenever the local discretization error estimated by a wavelet approximation exceeds a threshold. This threshold is set at $\epsilon_c = 0.01$ for the error on the volume fraction variable c and to $\epsilon_u = 0.1$ for the error on the velocity field. To investigate the influence

of the relatively large error level on the velocity we plot the histograms of droplet sizes at various error thresholds in Figure 18. On that Figure it is seen that although the total number of droplets changes significantly when ϵ_u decreases from 0.1 to 0.01, the position of the relative maxima and hence the typical droplet sizes vary relatively little. It is interesting to illustrate how grid adaptation interacts with ligament detection and perforation in the signature and manifold death methods. The signature method (Chirco *et al.* 2022) typifies the phase distribution with an index i_s . This index i_s is determined by the signature of the quadratic form of Chirco *et al.* (2022). In summary, i_s can take four values. The index $i_s = -1$ designates gas phase, the index $i_s = 2$ designates a liquid phase while the index $i_s = 0$ designates an interface. The fourth value that the index takes is $i_s = 1$ which designates a thin film region. Note that this detection is performed at the manifold death level and is later prolonged to the maximum level. Moreover the thin structure detection procedure acts without affecting the existing mesh refinement. Hence the mesh refinement is controlled only by the thresholds on the volume fraction and velocity field and in no way depends on the thin-sheet detection procedure. We illustrate the process of controlled sheet perforation using the manifold death method in Figure 19. We see that we have detected a thin region (red) in the upper image and a part of this region is eventually punctured in the lower image.

Appendix C. Estimates of the mass loss due to the manifold death

In the manifold death method, we artificially punch holes in thin structures. This results in some fluid disappearance and hence mass loss. Here we give an estimate of the mass loss for the case $(l, m) = (14, 13)$, that is the simulation corresponding to the red line in Figure 13b. Figure 20a shows how the total mass behaves as a function of time. It is a linear rise in time with a tiny sinusoidal pulsation caused by the injection condition. Since we punch holes in these structures every $t += 0.01$, a tiny decrease from this linear rise is expected every $+= 0.01$ interval. The inset zoomed at $t = 1.35$ shows this decrease in mass. The decrease is so small that it is not visible on the scale of the outer plot. To quantify this decrease, we calculate two quantities illustrated in the schematic of Figure 20b. The ΔM is the difference in the total mass at the timestamp just before punching a hole and the timestamp just after punching the hole. The plot as a function of time is shown in 20c, where the ΔM values are indicated every $t += 0.01$. Note that as mass is constantly being injected, this implies the number of thin structures shall increase with time and hence the ΔM is seen increasing with an oscillating behaviour. To get a non-dimensional estimate, we calculate the DIFF defined as

$$DIFF = 2M(i) - M(i - 1) - M(i + 1)$$

(see also the sketch in Fig. 20b) and calculate the percentage mass loss as

$$\text{Mass loss (\%)} = \frac{DIFF}{M[i]} \times 100. \quad (\text{C } 1)$$

The rationale of using DIFF over ΔM is that since we are injecting some liquid constantly, we want to estimate how the mass differs not only from the value just before punching holes, but from the expected value that it was supposed to have. The percentage loss is shown in Figure 20d, where we can see an exponential decrease in time. The plots 20c and 20d, together indicate that although the total mass of thin structures is increasing in time, the mass lost relative to the total mass is going to zero as the jet advances.

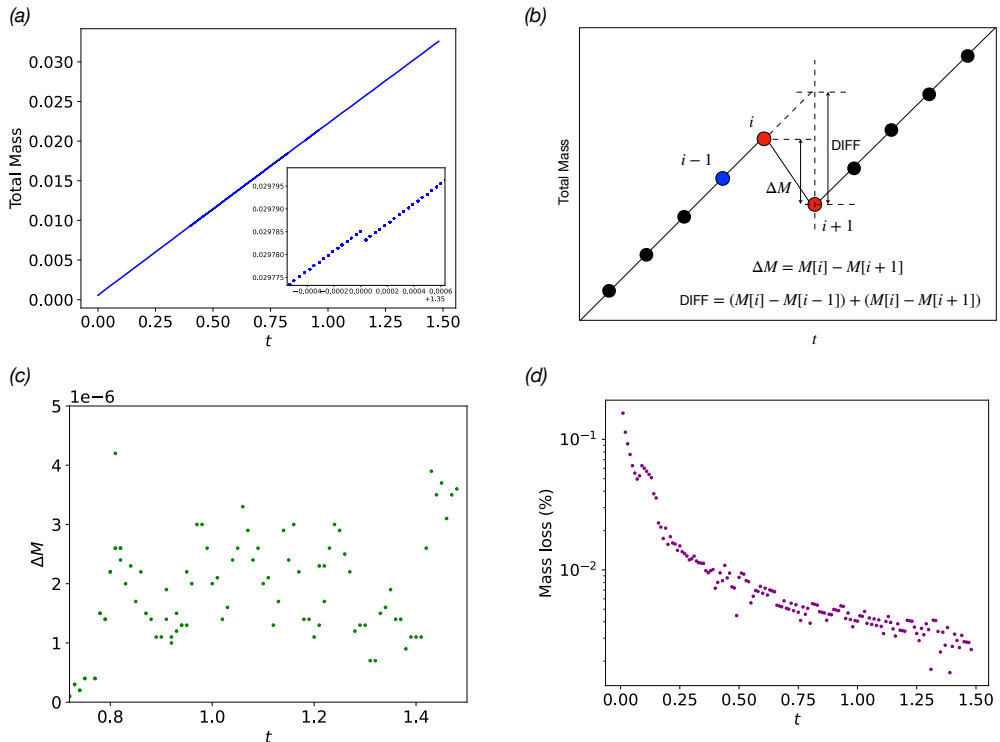


FIGURE 20. Estimates of the mass loss with manifold death performed at levels $(\ell, m) = (14, 13)$. (a) Total mass as a function of time. Inset shows the tiny droplet at time $t = 1.35$ due to artificial punching of thin structures every $t \pm 0.01$. (b) schematic of the data points and the procedure to estimate the mass loss. The value at i represents the mass just before punching the holes and the value at $i + 1$ represents the value just after punching the holes. ΔM and DIFF are used to do mass loss estimates. (c) ΔM at every $t \pm 0.01$. (d) Mass loss in percentage calculated as $\frac{\text{DIFF}}{M[i]} \times 100$.

Appendix D. Evolving initial mushroom: manifold death in action

Figure 21 shows the evolution of the initial mushroom jet and the first sheet rupture. Figure 21a shows the no-MD case at $\ell = 14$. We can see in the inset at $t = 0.15$, numerical sheet rupture happens in the flap connecting the rolled-up mushroom rim with the mushroom head. The inset shows how a spectrum of tiny droplets forms along with a circular ligament rim at $t = 0.17$. Figure 21b shows the first sheet rupture for the case with manifold death method applied, corresponding to $(\ell, m) = (15, 13)$, that the one corresponding to the blue line in Figure 13b. One can see the sheet rupture at $t = 0.11$ is much more clear now and the curvature oscillations are not present. In this case too we see detachment of the rolled up tip in form a circular ligament at $t = 0.17$. Simple analysis suggests that sheet thickness near the tip at the moment of rim formation should scale as D/We_g (see for example Marcotte & Zaleski (2019)). The condition $D/We_g \gg \Delta$ is then necessary for proper resolution of the sheet. This condition is equivalent to $We_\Delta \gg 1$ which is verified only for $\ell = 15$ and perhaps 14 according to Table 2. At lower levels, it is clear that numerical breakup may appear soon behind the rim in no-MD simulations.

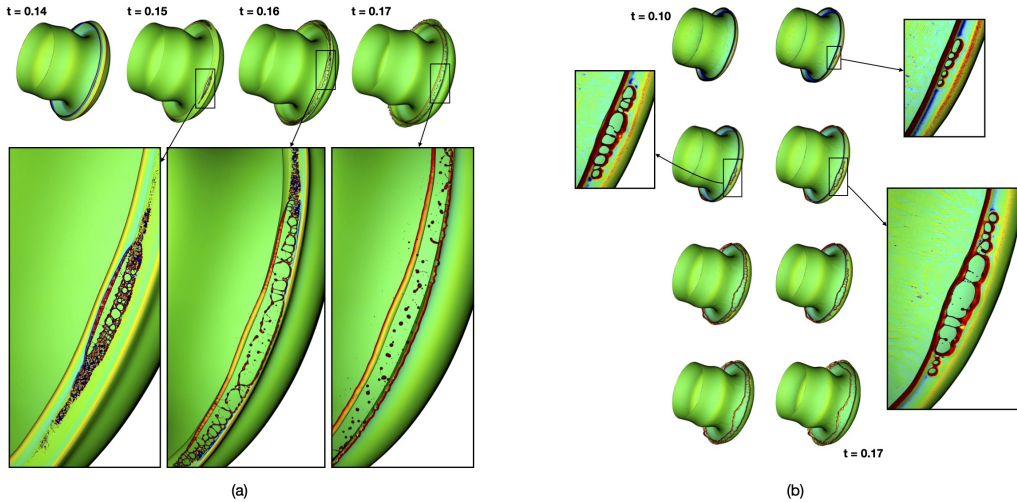


FIGURE 21. Evolution of the initial mushroom and the first breakup in (a) no manifold death and (b) with manifold death. The interface is colored by the curvature field in both cases. Image (a) shows a detailed view of the first numerical sheet rupture for an $\ell = 14$ simulation. Image (b) corresponds to the simulation with manifold death method applied corresponding to $(\ell, m) = (15, 13)$. The images shown in (b) are at time $t = 0.1, 0.11, 0.12, \dots, 0.17$. The detachment of a circular ligament rim is seen in both cases at $t = 0.17$.

Appendix E. Determination of d_c for manifold death statistics

The determination of d_c , that is the diameter marking the lower bound of the converged region is done by visual inspection of the histogram showing the droplet size distribution. Figure 22 shows a zoom-in explaining how we determine d_c for each consecutive level. Note that the black curve in the no-MD case is not overlapping in the converged region of the various MD simulations. This is an important fact since it means that an MD simulation is not “equivalent” to a no-MD simulation with a similar “effective” critical thickness h_c . Hence it makes more sense to compare the MD plots to each other and treat the black no-MD curves only for the purpose of analyzing the properties of classical non-converging simulations.

Appendix F. Forensics of the Chirco *et al.* (2022) study

The manifold death method appeared first in the work of Chirco *et al.* (2022). Here we revisit this previous study with the droplet size distribution comparison method described above. In Chirco *et al.* (2022) a region of convergence was identified at $8\Delta_9$ where Δ_9 was the grid size of the coarsest simulation, also used as the manifold death level. In our study, we have shown that the region of statistical convergence can be reached up to the critical sheet thickness of the manifold death threshold h_c , given that the mesh is refined sufficiently. In Figure 12 of Chirco *et al.* (2022), the authors argue that above $d_c = 8\Delta_9$, the simulations seem to converge, where the coarsest mesh had the equivalent of 512^3 cells ($\ell = 9$) and the finest mesh was the equivalent of 2048^3 cells ($\ell = 11$). The case that the authors simulated was a phase inversion case which produces a much smaller number of droplets than our pulsed jet case does. This implies that the number frequencies are affected by a large statistical error. Hence, the conclusions presented in Chirco *et al.* (2022) are qualitative: they demonstrate the rupture of the sheet by manifold death in a clear manner. To attempt a more quantitative analysis in line with our analysis of the

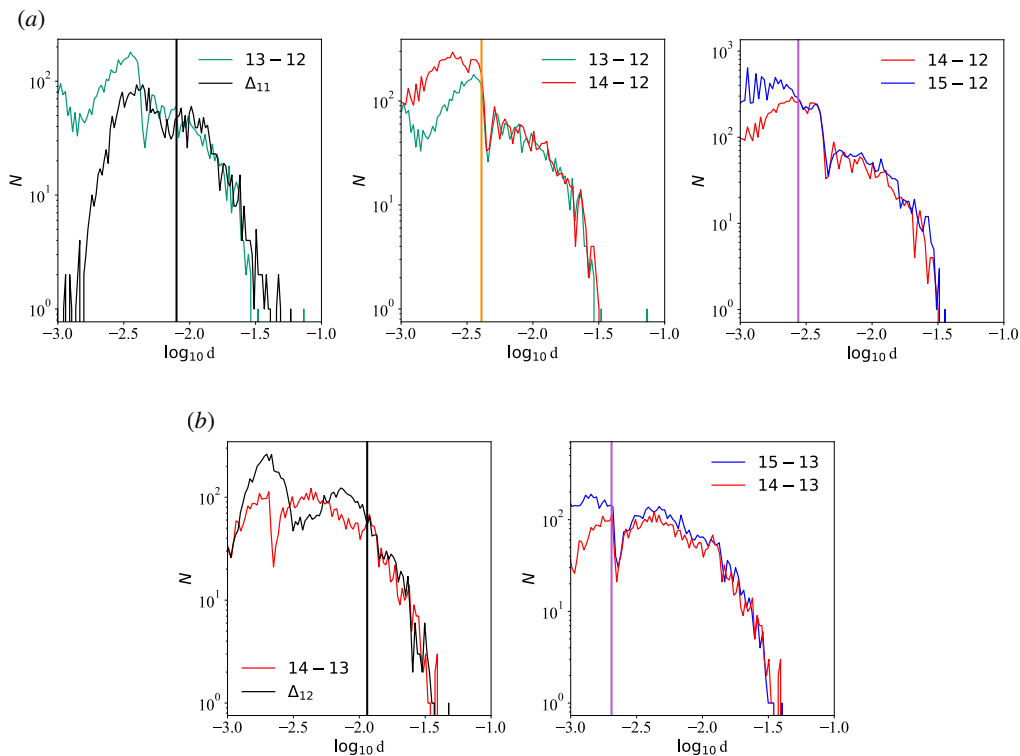


FIGURE 22. A zoom-in for the converged region corresponding to Figure 13 showing how d_c is obtained. Figures (a) and (b) correspond to a zoom-in for Figure 13a and 13b respectively.

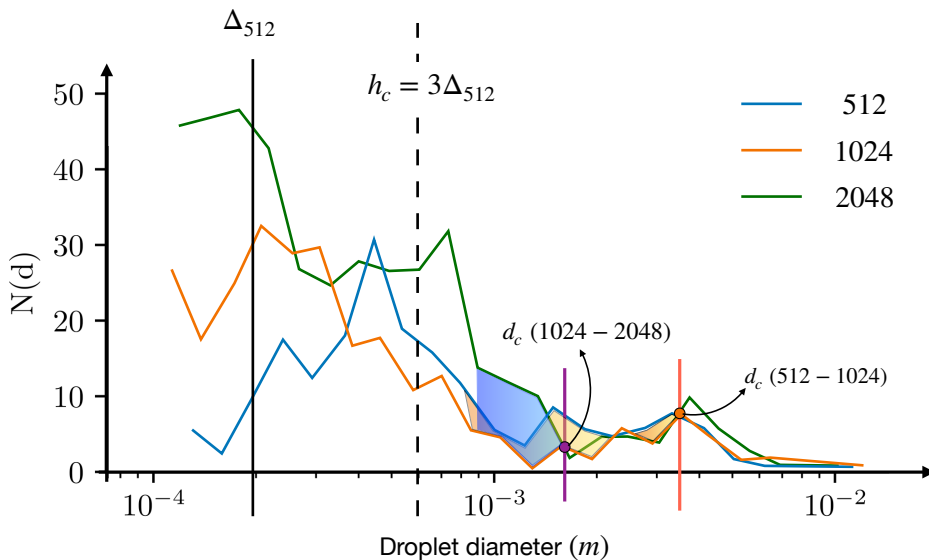


FIGURE 23. Replotting Figure 12 of Chirco *et al.* (2022) with additional vertical lines showing the critical thickness for manifold death sheet perforation threshold h_c , along with two vertical lines for d_c . The shaded regions illustrate the departure of the measured distribution from each other below d_c .

pulsed jet, we re-plot Figure 12 of Chirco *et al.* (2022) in our Figure 23. There we mark the MD threshold $h_c = 3\Delta_9$ and two values of d_c . We see that d_c again moves towards h_c . This movement is in line with our results. Due to computational cost, Chirco *et al.* (2022) stopped at the 2048^3 mesh and concluded that the boundary of the converged region lies at $d_c \sim 8\Delta_9$. It is likely that the converged region could be pushed more towards h_c with increased resolution.

REFERENCES

- ANEZ, J., AHMED, A., HECHT, N., DURET, B., REVELLON, J. & DEMOULIN, F. X. 2019 Eulerian–lagrangian spray atomization model coupled with interface capturing method for diesel injectors. *International Journal of Multiphase Flow* **113**, 325–342.
- BALACHANDAR, S., ZALESKI, S., SOLDATI, A., AHMADI, G. & BOURQUIBA, L. 2020 Host-to-host airborne transmission as a multiphase flow problem for science-based social distance guidelines. *International Journal of Multiphase Flow* **132**, 103439.
- BEN RAYANA, F., CARTELLIER, A. & HOPFINGER, E. 2006 Assisted atomization of a liquid layer: investigation of the parameters affecting the mean drop size prediction. In *Proc. ICLASS 2006, Aug. 27-Sept.1, Kyoto Japan*. Academic Publ. and Printings, ISBN4-9902774-1-4.
- BIANCHI, G. M., PELLONI, P., TONINEL, S., SCARDOVELLI, R., LEBOSSETIER, A. & ZALESKI, S. 2005 A quasi-direct 3D simulation of the atomization of high-speed liquid jets. In *Proceedings of ICES05, 2005 ASME ICE Division Spring Technical Conference*. Chicago, Illinois, USA, April 5-7, 2005.
- BORNIA, G., CERVONE, A., MANSERVISI, S., SCARDOVELLI, R. & ZALESKI, S. 2011 On the properties and limitations of the height function method in two-dimensional cartesian geometry. *J. Comput. Phys.* **230**, 851–862.
- CHESNEL, J., MÉNARD, T., RÉVELLON, J. & DEMOULIN, F.-X. 2011 Subgrid analysis of liquid jet atomization. *Atomization and Sprays* **21** (1).
- CHIRCO, L., MAAREK, J., POPINET, S. & ZALESKI, S. 2022 Manifold death: A volume of fluid implementation of controlled topological changes in thin sheets by the signature method. *Journal of Computational Physics* **467**, 111468.
- CHORIN, A. J. 1968 Numerical solution of the Navier–Stokes equation. *Mathematics of Computing* **22**, 745–762.
- CULICK, F. E. C. 1960 Comments on a ruptured soap film. *J. Appl. Phys.* **31**, 1128–1129.
- DEBAR, R. 1974 Fundamentals of the KRAKEN code. *Tech. Rep. UCIR-760*. LLNL.
- DEBRÉGEAS, G. D., DE GENNES, P.-G. & BROCHARD-WYART, F. 1998 The life and death of “bare” viscous bubbles. *Science* **279** (5357), 1704–1707.
- DUKE, D. J., KASTENGREN, A. L., MATUSIK, K. E., SWANTEK, A. B., POWELL, C. F., PAYRI, R., VAQUERIZO, D., ITANI, L., BRUNEAUX, G., GROVER JR, R. O. & OTHERS 2017 Internal and near nozzle measurements of engine combustion network “Spray G” gasoline direct injectors. *Experimental Thermal and Fluid Science* **88**, 608–621.
- FUSTER, D., BAGUÉ, A., BOECK, T., LE MOYNE, L., LEBOSSETIER, A., POPINET, S., RAY, P., SCARDOVELLI, R. & ZALESKI, S. 2009 Simulation of primary atomization with an octree adaptive mesh refinement and VOF method. *International Journal of Multiphase Flow* **35** (6), 550–565.
- FUSTER, D., MATAS, J. P., MARTY, S., POPINET, S., HOEPFFNER, J., CARTELLIER, A. & ZALESKI, S. 2013 Instability regimes in the primary breakup region of planar coflowing sheets. *Journal of Fluid Mechanics* **736**, 150–176.
- GOROKHOVSKI, M. & HERRMANN, M. 2008 Modeling Primary Atomization. *Annual Reviews of Fluid Mechanics* pp. 343–366.
- HERRMANN, M. 2010 A parallel eulerian interface tracking/lagrangian point particle multi-scale coupling procedure. *Journal of Computational Physics* **229** (3), 745–759.
- HERRMANN, M. 2011 On simulating primary atomization using the refined level set grid method. *Atomization and Sprays* **21** (4), 283–301.
- HIRT, C.W. & NICHOLS, B.D. 1981 Volume of fluid (VOF) method for the dynamics of free boundaries. *Journal of Computational Physics* **39** (1), 201–225.

- JACKIW, I. M. & ASHGRIZ, N. 2022 Prediction of the droplet size distribution in aerodynamic droplet breakup. *Journal of Fluid Mechanics* **940**, A17.
- JARRAHBASHI, D. & SIRIGNANO, W. A. 2014 Invited Article: Vorticity dynamics for transient high-pressure liquid injection. *Physics of Fluids* **26** (10).
- JARRAHBASHI, D., SIRIGNANO, W. A., POPOV, P. P. & HUSSAIN, F. 2016 Early spray development at high gas density: hole, ligament and bridge formations. *Journal of Fluid Mechanics* **792**, 186–231.
- JIANG, D & LING, Y 2021 Impact of inlet gas turbulence on the formation, development and breakup of interfacial waves in a two-phase mixing layer. *Journal of Fluid Mechanics* **921**, A15.
- KANT, P., PAIRETTI, C., SAADE, Y., POPINET, S., ZALESKI, S. & LOHSE, D. 2023 Bag-mediated film atomization in a cough machine. *Phys. Rev. Fluids* **8** (7), 074802.
- KHANWALE, M. A, SAURABH, K., ISHII, M., SUNDAR, H. & GANAPATHYSUBRAMANIAN, B. 2022 Breakup dynamics in primary jet atomization using mesh-and interface-refined cahn-hilliard navier-stokes. *arXiv preprint arXiv:2209.13142* .
- KIBBLE, T. W. B. 1976 Topology of cosmic domains and strings. *Journal of Physics A: Mathematical and General* **9** (8), 1387.
- LASHERAS, J. C. & HOPFINGER, E. J. 2000 Liquid jet instability and atomization in a coaxial gas stream. *Annu. Rev. Fluid Mech.* **32**, 275–308.
- LEBAS, R., MENARD, T., BEAU, P.A., BERLEMONT, A. & DEMOULIN, FRANÇOIS-XAVIER 2009 Numerical simulation of primary break-up and atomization: DNS and modelling study. *International Journal of Multiphase Flow* **35** (3), 247–260.
- LING, Y., FUSTER, D., ZALESKI, S. & TRYGGVASON, G. 2017 Spray formation in a quasiplanar gas–liquid mixing layer at moderate density ratios: A numerical closeup. *Phys. Rev. Fluids* **2** (1), 014005.
- LOHSE, D. & VILLERMAUX, E. 2020 Double threshold behavior for breakup of liquid sheets. *Proceedings of the National Academy of Sciences* **117** (32), 18912–18914.
- MARCOTTE, F. & ZALESKI, S. 2019 Density contrast matters for drop fragmentation thresholds at low Ohnesorge number. *Phys. Rev. Fluids* **4** (10), 103604.
- MATAS, JEAN-PHILIPPE, MARTY, SYLVAIN & CARTELLIER, ALAIN 2011 Experimental and analytical study of the shear instability of a gas-liquid mixing layer. *Physics of fluids* **23** (9), 094112.
- MÉNARD, T., TANGUY, S. & BERLEMONT, A. 2007 Coupling level set/VOF/ghost fluid methods: Validation and application to 3D simulation of the primary break-up of a liquid jet. *Int. J. of Multiphase Flow* **33** (5), 510–524.
- OPFER, L., ROISMAN, I.V., VENZMER, J, KLOSTERMANN, M. & TROPEA, C. 2014 Droplet-air collision dynamics: Evolution of the film thickness. *Phys. Rev. E* **89** (1), 013023.
- PAIRETTI, CESAR, VILLIERS, RAPHAËL & ZALESKI, STÉPHANE 2021 A numerical cough machine. Accepted for publication in *Computer and Fluids*.
- PAIRETTI, C. I., DAMIAN, S. M., NIGRO, N. M, POPINET, S. & ZALESKI, S. 2020 Mesh resolution effects on primary atomization simulations. *Atomization and Sprays* **30** (12).
- POPINET, S. 2003 Gerris: a tree-based adaptive solver for the incompressible euler equations in complex geometries. *J. Comput. Phys.* **190** (2), 572–600.
- POPINET, S. 2009 An accurate adaptive solver for surface-tension-driven interfacial flows. *J. Comput. Phys.* **228** (16), 5838–5866.
- POPINET, S. 2018 Numerical Models of Surface Tension. *Annu. Rev. Fluid Mech.* **50** (1), 49–75, arXiv: 1507.05135.
- SALVADOR, F. J., RUIZ, S., CRIALESI-ESPOSITO, M. & BLANQUER, I. 2018 Analysis on the effects of turbulent inflow conditions on spray primary atomization in the near-field by direct numerical simulation. *Int. J. of Multiphase Flow* **102**, 49–63.
- SAURABH, K., ISHII, M., KHANWALE, M. A, SUNDAR, H. & GANAPATHYSUBRAMANIAN, B. 2023 Scalable adaptive algorithms for next-generation multiphase flow simulations. In *2023 IEEE International Parallel and Distributed Processing Symposium (IPDPS)*, pp. 590–601. IEEE.
- SAVVA, N. & BUSH, J. W. M. 2009 Viscous sheet retraction. *J. Fluid Mech.* **626**, 211–240.
- SHINJO, J & UMEMURA, A 2010 Simulation of liquid jet primary breakup: Dynamics of ligament and droplet formation. *International Journal of Multiphase Flow* **36** (7), 513–532.

- SONG, M. & TRYGGVASON, G. 1999 The formation of thick borders on an initially stationary fluid sheet. *Phys. Fluids* **11** (9), 2487–93.
- TANG, K., ADCOCK, T.A.A. & MOSTERT, W. 2023 Bag film breakup of droplets in uniform airflows. *Journal of Fluid Mechanics* **970**, A9.
- TAYLOR, G. I. 1959 The dynamics of thin sheets of fluid III. Disintegration of fluid sheets. *Proc. Roy. Soc. London A* **253**, 313–321.
- TORREGROSA, A. J., PAYRI, R., SALVADOR, F. J. & CRIALESI-ESPOSITO, M. 2020 Study of turbulence in atomizing liquid jets. *International Journal of Multiphase Flow* **129**, 103328.
- VILLERMAUX, E. 2020 Fragmentation versus cohesion. *J. Fluid Mech.* **898**.
- VILLERMAUX, E & BOSSA, B 2009 Single-drop fragmentation determines size distribution of raindrops. *Nature Physics* .
- WANG, Y & BOURQUIBA, L 2018 Unsteady sheet fragmentation: droplet sizes and speeds. *J. Fluid Mech.* **848**, 946–967.
- WEYMOUTH, G. D. & YUE, D. K. P. 2010 Conservative Volume-of-Fluid method for free-surface simulations on Cartesian-grids. *J. Comput. Phys.* **229** (8), 2853–2865.
- ZHANG, B., POPINET, S. & LING, Y. 2020 Modeling and detailed numerical simulation of the primary breakup of a gasoline surrogate jet under non-evaporative operating conditions. *Int. J. of Multiphase Flow* **130**, 103362.
- ZUREK, W. H. 1985 Cosmological experiments in superfluid helium? *Nature* **317** (6037), 505–508.